INVERSE PROBLEMS IN SCIENCE AND ENGINEERING, 2017
VOL. 25, NO. 6, 832–863
http://dx.doi.org/10.1080/17415977.2016.1201663

Taylor & Francis
Taylor & Francis Group

An inverse-source problem for maximization of pore-fluid oscillation within poroelastic formations

C. Jeong[a] and L. F. Kallivokas[b]

[a]Department of Civil Engineering, The Catholic University of America, Washington, DC, USA; [b]Department of Civil, Architectural and Environmental Engineering, The University of Texas at Austin, Austin, TX, USA

ABSTRACT

This paper discusses a mathematical and numerical modeling approach for identification of an unknown optimal loading time signal of a wave source, atop the ground surface, that can maximize the relative wave motion of a single-phase pore fluid within fluid-saturated porous permeable (poroelastic) rock formations, surrounded by non-permeable semi-infinite elastic solid rock formations, in a one-dimensional setting. The motivation stems from a set of field observations, following seismic events and vibrational tests, suggesting that shaking an oil reservoir is likely to improve oil production rates. This maximization problem is cast into an inverse-source problem, seeking an optimal loading signal that minimizes an objective functional – the reciprocal of kinetic energy in terms of relative pore-fluid wave motion within target poroelastic layers. We use the finite element method to obtain the solution of the governing wave physics of a multi-layered system, where the wave equations for the target poroelastic layers and the elastic wave equation for the surrounding non-permeable layers are coupled with each other. We use a partial-differential-equation-constrained-optimization framework (a state-adjoint-control problem approach) to tackle the minimization problem. The numerical results show that the numerical optimizer recovers optimal loading signals, whose dominant frequencies correspond to amplification frequencies, which can also be obtained by a frequency sweep, leading to larger amplitudes of relative pore-fluid wave motion within the target hydrocarbon formation than other signals.

ARTICLE HISTORY
Received 26 August 2015
Accepted 11 June 2016

KEYWORDS
Wave-based enhanced oil recovery; pore-fluid oscillation; poroelastic solids; PDE-constrained optimization; amplification frequencies; inverse-source problem; pore-fluid flow hysteresis model

AMS SUBJECT CLASSIFICATIONS
74J25; 74F10; 86A22

1. Introduction

1.1. Vibrational stimulation for enhanced oil recovery

Persistent global demand for hydrocarbon energy sources, coupled with the difficulties associated with the exploration and exploitation of new hydrocarbon reserves, has renewed emphasis on improving the efficiency of oil recovery from existing reservoirs by using enhanced oil recovery methods.[1] In order to recover any oil still remaining in an existing reservoir, EOR methods, such as gas- and polymer-flooding, are usually employed.[2,3]

CONTACT C. Jeong jeong@cua.edu

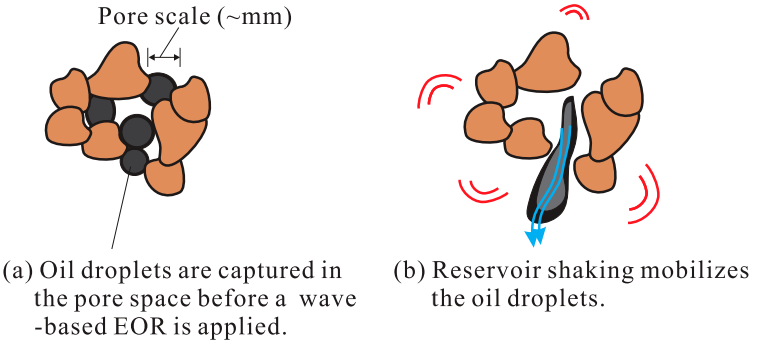

Figure 1. The mobilization of trapped oil droplets in pore space by the vibration of the pore wall surface.

The wave-based EOR method has been proposed as one cost-effective EOR method. The key idea behind the wave-based EOR method is that traveling waves, however they may be generated, could 'shake' a reservoir sufficiently to mobilize the remaining oil, which could then be recovered by conventional means. Wave sources typically used in the wave-based EOR include Vibroseis equipments atop the ground surface,[4–7] wellbore hydraulic pumps,[8] or wellbore seismic vibrators.[9,10] All sources are capable of generating, directly or indirectly, elastic waves. The wave-based EOR is considered to be as effective as conventional EOR methods because elastic waves can indiscriminately illuminate the entire volume of an oil reservoir, whereas, due to the heterogeneity of a typical reservoir, gas- or chemical-flooding can hardly sweep it in its entirety.

The feasibility of the wave-based EOR is supported by a set of field observations showing that elastic waves induce increased production of the remaining oil.[11–24] It has been also reported that the seismic waves increase permeability within hydrocarbon formations. Elkhoury et al. [25] presented that seismic waves can alter the permeability of aquifers. The laboratory tests that use fluid flow oscillation of a very low frequency (0.05 Hz) showed that permeability within a fractured rock can be improved by vibrational stimulation.[26] Geballe et al. [27] and Manga et al. [28] suggested that unblocking pore spaces, by vibrationally breaking colloidal deposits or mobilizing droplets trapped in pores, contribute to the change of permeability.

As one suggested predominant mechanism of the wave-based EOR, the movement of the pore walls can mobilize oil droplets trapped in pore spaces.[29–32] That is, the vibration of pore walls can dislodge the trapped droplets and coalesce them into larger ones, allowing them to be mobilized and flow (see the illustration in Figure 1). A set of experimental studies support this mechanism.[22,30,33–41] In addition, Iassonov and Beresnev [42] developed a threshold capillary-trapping model: an inertial force, induced by the elastic wave on a trapped oil droplet, should exceed a threshold level in order for the trapped oil droplet to overcome the capillary force. Subsequent experiments [43,44] and numerical simulations [45–47] presented that the acceleration of the rock matrix should be in the order of 0.1 m/s^2 or more to induce oil mobilization. Jeong et al. [48,49] showed that a fleet of sufficiently strong wave sources should be employed to generate such large acceleration of rock matrix because wave response attenuates quickly with respect to the traveling distance, largely due to geometric and intrinsic attenuations.

On the other hand, it has been argued that reservoir shaking can lead to oscillatory cross-flow at the interfaces between low and high permeability areas in a highly heterogeneous

reservoir or in a fractured reservoir.[50–55] In a heterogeneous reservoir, the elastic waves induce pore-pressure oscillation between layers of different permeability [50,52] Such pressure oscillation could effectively coax out bypassed oil from the low to high permeability areas. In a fractured reservoir, the direct application of hydraulic wave sources to a fracture can induce periodic pressure gradient at the interface wall between a fracture and its surrounding rock matrix such that the transport of bypassed oil from the rock matrix to the fracture space is facilitated.[48,51,53–56]

1.2. Inverse-source problems for the wave-based EOR

To examine the possibility of maximizing the outcome of the wave-based EOR, we have investigated the feasibility of identifying unknown optimal source conditions that can maximize desired metrics for the wave-induced EOR. To this end, we have formulated the associated mathematical problem as an inverse-source problem.[1] [48,49,61,62] That is, for a known geostructure, containing a target formation (reservoir), one seeks to determine the input excitations that will maximize desired outcomes, e.g. wave energy at the reservoir, while minimizing undesired metrics, e.g. vibrational disturbance in surrounding formations. The geostructure is considered arbitrarily heterogeneous as the target hydrocarbon rock formations are surrounded by non-permeable rock formations. Sources are deployed on the ground surface (if needed, within the wellbore for a deep reservoir). Due to the semi-infinite extent of the physical domain, an absorbing boundary condition is used to truncate the physical domain in order to render it finite and, thus, computationally feasible.[5,63–65]

In our inverse-source problem studies, we have sought to maximize a desired metric by casting the problem as minimization of the metric's reciprocal. We have used the apparatus of *partial-differential-equation(PDE)-constrained-optimization* [66] in order to resolve the minimization problem with respect to a large set of control parameters, i.e. variables used for the parameterization of unknown optimal time signals of multiple wave sources. In mathematical terms, we defined a Lagrangian, comprising a reciprocal functional describing the metric sought to be maximized, augmented by the side-imposition of the problem's governing physics PDEs. Satisfaction of the first-order optimality conditions leads to a triad of state, adjoint, and control problems. We numerically resolved the state and adjoint problems, and used the control problem to update control parameters until convergence. Jeong et al. [61] presented a source-inversion method for identifying an unknown optimal loading time signal of a ground surface wave source, leading to focusing of kinetic energy or maximization of acceleration of the solid rock matrix in a selected formation in a one-dimensional elastic solid setting. The numerical optimizer identifies optimal loading time signals with strong dominant frequency components that coincide with the exact or analytically-computed amplification frequencies. It was shown that there are a set of amplification frequencies that lead to large rock wave motion in the targeted formation. A different set of amplification frequencies can also selectively maximize the wave energy within the target layer, while the adjacent formations stay relatively dormant (i.e. wave energy focusing). The source-inversion approach continued in a more realistic two-dimensional elastic wave setting,[49,62,67–70] showing that focusing wave energy into a hydrocarbon reservoir is feasible by employing the optimal locations and excitation time signals of the wave sources that can maximize desired metrics (such as wave energy within targeted reservoir formations) and minimize undesired metrics (e.g. vibrational

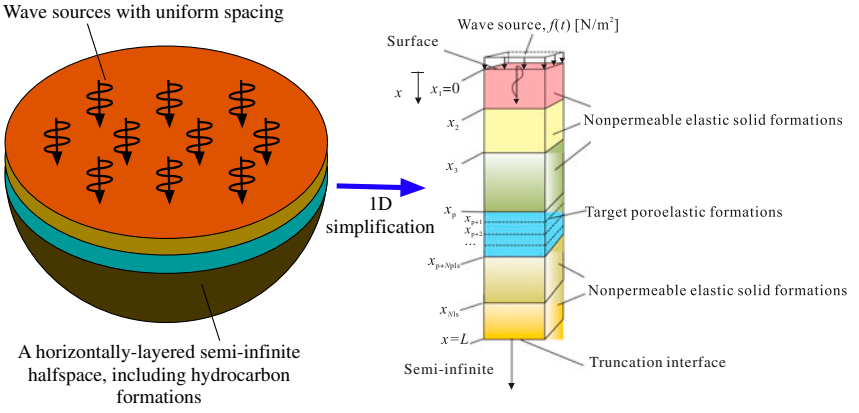

Figure 2. Targeted fluid-saturated porous permeable rock formations embedded within a one-dimensional semi-infinite non-permeable elastic solid media system; truncated at depth $x = L$, subject to a surface excitation.

disturbance within adjacent formation areas). Following the preceding source-inversion studies, in this paper, we are concerned with maximizing the pore fluid wave motion within a more realistic target, that of a poroelastic formation. Specifically, this work aims at maximizing the relative motion of the pore fluid with respect to the solid matrix because the relative motion of a trapped oil droplet with respect to the solid channel is used to define the extraction threshold in pore-scale studies.[47]

As a prototype, we will consider a porous permeable rock formation, saturated by a single-phase fluid, that is surrounded by non-permeable elastic rock formations of the semi-infinite extent in the one-dimensional setting. To obtain the wave behavior of the pore fluid and rock matrix within poroelastic media, we numerically address the wave equations for poroelastic solids fully saturated by a single-phase fluid.[71–76] We adopt the u–w finite element formulation,[73,75,76] which was verified against analytical solutions.[74] It should be noted that, in realistic reservoir settings, reservoir formations are fully or partially saturated by multi-phase fluids, i.e. oil, gas, and water.[77–82] Despite the gap between the presented prototype setting and the realistic one in a hydrocarbon reservoir, this work can provide insight into the following questions:

- Is it feasible to identify wave source conditions, such as loading time signals, that can maximize the relative wave motion of the pore fluid in poroelastic formations using the PDE-constrained optimization framework? Do the source-inversion results yield the essential characteristics of the optimal wave sources?

The answers to the questions from this work could provide proof of concept and scale to more realistic settings. In summary:

- This paper describes a state-adjoint-control triplet approach for the identification of an unknown wave source's optimal loading signal, that can maximize the relative wave motion of a single-phase pore fluid within a target poroelastic formation surrounded by non-permeable elastic solid formations of semi-infinite extent. As will be shown, the developed numerical optimizer results in loading signals, whose dominant frequencies coincide with the amplification frequencies that correspond to the maximum relative wave motion of the pore fluid.

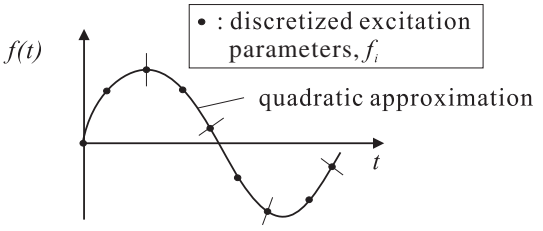

Figure 3. Schematic of parameterization of the unknown excitation $f(t)$ using quadratic shape functions.

2. Problem definition

2.1. Governing wave physics

We consider wave motion in target fluid-saturated porous permeable elastic solid (poroelastic) layers that are surrounded by non-permeable elastic solid layers (see Figure 2). The semi-infinite extent of the original domain is truncated through the introduction of an absorbing boundary at some depth $x = L$. The propagation of waves within the coupled system ($\Omega = (0, L)$) is governed by the following PDEs (for brevity, the space and time dependency of the variables and coefficients are dropped):

$$\frac{\partial}{\partial x}\left((\lambda + 2\mu)\frac{\partial u_{\mathrm{a}}}{\partial x}\right) - \rho\frac{\partial^2 u_{\mathrm{a}}}{\partial t^2} = 0, \qquad x \in \Omega \setminus \Omega_{\mathrm{p}}, \quad t \in (0, T], \tag{1}$$

$$\frac{\partial}{\partial x}\left((\lambda + 2\mu + \alpha^2 Q)\frac{\partial u_{\mathrm{b}}}{\partial x} + \alpha Q\frac{\partial w}{\partial x}\right) - \rho\frac{\partial^2 u_{\mathrm{b}}}{\partial t^2} - \rho_f\frac{\partial^2 w}{\partial t^2} = 0, \qquad x \in \Omega_{\mathrm{p}}, \ t \in (0, T], \tag{2}$$

$$\frac{\partial}{\partial x}\left(\alpha Q\frac{\partial u_{\mathrm{b}}}{\partial x} + Q\frac{\partial w}{\partial x}\right) - \frac{1}{k}\frac{\partial w}{\partial t} - \rho_f\frac{\partial^2 u_{\mathrm{b}}}{\partial t^2} - \frac{\rho_f}{n}\frac{\partial^2 w}{\partial t^2} = 0, \qquad x \in \Omega_{\mathrm{p}}, \quad t \in (0, T]. \tag{3}$$

Equation (1) is the equation of motion for a compressional wave in the elastic solid layers ($x \in (\Omega \setminus \Omega_{\mathrm{p}})$), i.e. $(0, x_p)$ and $(x_{p+N_{\mathrm{pls}}}, L)$. Equations (2) and (3) are the coupled wave equations for poroelastic solid layers ($x \in \Omega_{\mathrm{p}}$), i.e. $(x_p, x_{p+N_{\mathrm{pls}}})$, fully saturated by a single-phase fluid[2] [71–75]; Equation (2) is the equation of motion for the solid-fluid mixture [74]; Equation (3) is Darcy's law for the solid-fluid mixture.[74,83]

In (1)–(3), x denotes location, and t denotes time; x_i denotes the x-directional depth of a boundary or an interface atop the i-th layer, whereby x_p and $x_{p+N_{\mathrm{pls}}}$ denote the locations of the two interfaces between the non-permeable elastic solid layers and the poroelastic layers; the subscript p denotes the layer index of the top poroelastic formation; and the subscript N_{pls} denotes the total number of the poroelastic layers. T denotes the total observation duration. $u_{\mathrm{a}}(x, t)$ denotes the displacement of the non-permeable elastic solid formations; $u_{\mathrm{b}}(x, t)$ denotes the displacement of the solid rock matrix of the poroelastic formations; and $w(x, t)$ denotes the relative displacement of pore-fluid motion with respect to the rock matrix. The material parameters, used in (1)–(3), are defined as follows:

Elastic wave equation (1)

- λ: Lamé's first parameter of elastic solid, $\lambda = \frac{\nu E}{(1+\nu)(1-2\nu)}$,
- μ: Shear modulus of elastic solid, $\mu = \frac{E}{2(1+\nu)}$,
- E: Elastic modulus of elastic solid,
- ν: Poisson's ratio of elastic solid,
- ρ: Mass density of elastic solid,

Biot's wave equations (2) and (3)

- λ: Lamé's first parameter of solid rock matrix, $\lambda = \frac{\nu E}{(1+\nu)(1-2\nu)}$,
- μ: Shear modulus of solid rock matrix, $\mu = \frac{E}{2(1+\nu)}$,
- E: Elastic modulus of solid rock matrix,
- ν: Poisson's ratio of solid rock matrix,
- ρ: Mass density of fluid-solid mixture, i.e. $\rho = (1-n)\rho_s + n\rho_f$,
- ρ_s: Mass density of solid rock matrix,
- ρ_f: Mass density of pore fluid,
- k: Fluid mobility, i.e. $k = \bar{k}/\eta$, as shown in [83],
- $\bar{k}$: Permeability,
- η: Viscosity of pore fluid,
- n: Porosity,
- α: Biot's material parameter, i.e. $\alpha = 1 - \frac{K_D}{K_S}$, where $n \leq \alpha \leq 1$,
- Q: Biot's material parameter, i.e. $Q = 1/\left(\frac{n}{K_f} + \frac{\alpha - n}{K_S}\right)$, where $0 < Q \leq \infty$,
- K_D: Bulk modulus of drained solid rock matrix, i.e. $K_D = \frac{E}{3(1-2\nu)}$,
- K_S: Bulk modulus of undrained solid rock matrix, i.e. $K_s = K_D/(1-\alpha)$,
- K_f: Bulk modulus of pore fluid.

In a fluid-saturated poroelastic medium, the following equation holds:

$$\sigma(x,t) = \sigma'(x,t) - \alpha P(x,t), \tag{4}$$

where $\sigma(x,t)$ denotes total stress; $\sigma'(x,t)$ denotes effective stress; and $P(x,t)$ denotes pore pressure, where $P(x,t)$ is positive for compression. $\sigma(x,t)$ and $P(x,t)$ are obtained from the displacement fields $u_{\mathrm{b}}(x,t)$ and $w(x,t)$ via the following constitutive equations:

$$\sigma = \left(\lambda + 2\mu + \alpha^2 Q\right)\frac{\partial u_{\mathrm{b}}}{\partial x} + \alpha Q \frac{\partial w}{\partial x}, \tag{5a}$$

$$P = -\left(\alpha Q \frac{\partial u_{\mathrm{b}}}{\partial x} + Q\frac{\partial w}{\partial x}\right). \tag{5b}$$

In addition, the governing PDEs are subject to the following boundary and truncation interface conditions:

$$(\lambda(0) + 2\mu(0))\frac{\partial u_{\mathrm{a}}}{\partial x}(0,t) = -f(t), \quad t \in (0,T], \tag{6}$$

$$\frac{\partial u_{\mathrm{a}}}{\partial x}(L,t) + \frac{1}{c(L)}\frac{\partial u_{\mathrm{a}}}{\partial t}(L,t) = 0, \quad t \in (0,T]. \tag{7}$$

Equation (6) is the surface excitation boundary condition; (7) is the truncation interface condition with $c = \sqrt{\frac{\lambda+2\mu}{\rho}}$. The governing wave physics also includes zero initial conditions.

The elastic wave equation (1), as well as the wave equations for the poroelastic layers (2) and (3) are coupled via the following conditions at the interfaces between the elastic solid layers and the poroelastic layers:

$$\begin{aligned} u_{\mathrm{a}}\big|_{x_i^-} &= u_{\mathrm{b}}\big|_{x_i^+}, \qquad i = p, \\ u_{\mathrm{a}}\big|_{x_i^+} &= u_{\mathrm{b}}\big|_{x_i^-}, \qquad i = (p + N_{\mathrm{pls}}), \end{aligned} \tag{8a}$$

$$(\lambda + 2\mu)\frac{\partial u_{\mathrm{a}}}{\partial x}\bigg|_{x_i^-} = (\lambda + 2\mu + \alpha^2 Q)\frac{\partial u_{\mathrm{b}}}{\partial x} + \alpha Q \frac{\partial w}{\partial x}\bigg|_{x_i^+}, \quad i = p, \tag{8b}$$

$$(\lambda + 2\mu)\frac{\partial u_{\mathrm{a}}}{\partial x}\bigg|_{x_i^+} = (\lambda + 2\mu + \alpha^2 Q)\frac{\partial u_{\mathrm{b}}}{\partial x} + \alpha Q \frac{\partial w}{\partial x}\bigg|_{x_i^-}, \quad i = (p + N_{\mathrm{pls}}), \tag{8b}$$

$$w\big|_{x_i} = 0, \quad i = p \text{ and } (p + N_{\mathrm{pls}}). \tag{8c}$$

Equations (8a) and (8b) are the rock matrix displacement and the total stress interface continuity conditions, respectively. Equation (8c) denotes the zero relative displacement of the pore fluid at the interfaces – (8c) is tantamount to the zero flux condition, i.e. $\frac{\partial P}{\partial x} = 0$.

Although the aforementioned governing PDEs can accommodate arbitrary heterogeneity of the material parameters, we explicitly consider a multi-layered system. For multi-layered elastic solid media, there hold the following continuity conditions of displacements and tractions at the interfaces between the mutually-adjacent elastic solid layers (i.e. interface indices: $i = (2, \ldots, (p-1))$ and $((p + N_{\mathrm{pls}} + 1), \ldots, N_{\mathrm{ls}})$):

$$u_{\mathrm{a}}\big|_{x_i^-} = u_{\mathrm{a}}\big|_{x_i^+} \quad , \tag{9a}$$

$$(\lambda + 2\mu)\frac{\partial u_{\mathrm{a}}}{\partial x}\bigg|_{x_i^-} = (\lambda + 2\mu)\frac{\partial u_{\mathrm{a}}}{\partial x}\bigg|_{x_i^+} \quad , \tag{9b}$$

where N_{ls} denotes the total number of all layers in the system. In addition, the following continuity conditions hold at the interfaces within poroelastic layers (i.e. interface indices: $i = (p+1), \ldots, (p + N_{\mathrm{pls}} - 1)$) :

$$u_{\mathrm{b}}\big|_{x_i^-} = u_{\mathrm{b}}\big|_{x_i^+}, \tag{10a}$$

$$w\big|_{x_i^-} = w\big|_{x_i^+}, \tag{10b}$$

$$(\lambda + 2\mu + \alpha^2 Q)\frac{\partial u_{\mathrm{b}}}{\partial x} + \alpha Q \frac{\partial w}{\partial x}\bigg|_{x_i^-} = (\lambda + 2\mu + \alpha^2 Q)\frac{\partial u_{\mathrm{b}}}{\partial x} + \alpha Q \frac{\partial w}{\partial x}\bigg|_{x_i^+}, \tag{10c}$$

$$\alpha Q \frac{\partial u_{\mathrm{b}}}{\partial x} + Q \frac{\partial w}{\partial x}\bigg|_{x_i^-} = \alpha Q \frac{\partial u_{\mathrm{b}}}{\partial x} + Q \frac{\partial w}{\partial x}\bigg|_{x_i^+}, \tag{10d}$$

where (10a) and (10b) denote the continuity of rock matrix displacement and relative displacement of pore fluid, respectively; (10c) denotes the continuity of total stress; and (10d) denotes the continuity of pore pressure.

2.2. Objective functional

We attempt to identify an optimal loading time signal that maximizes the kinetic energy[3] only in terms of $w(x,t)$, which is the relative displacement of the pore fluid with respect to the solid rock matrix.

To this end, we minimize the following objective functional:

$$\mathcal{L} = \frac{1}{\int_{\Omega_p}\int_0^T \rho_f \left(\frac{\partial w}{\partial t}(x,t)\right)^2 \mathrm{d}t\mathrm{d}x}. \tag{11}$$

Equation (11) is a reciprocal form, of which denominator is the temporal integral of the kinetic energy, in terms of $w(x,t)$, that is spatially integrated over the poroelastic layers (Ω_p) – we omit $\frac{1}{2}$ of the kinetic energy $\frac{\rho_f}{2}\left(\frac{\partial w}{\partial t}\right)^2$ because such an omission does not affect the optimized result of the loading time signal.

2.3. Wave source parameterization

We consider an unknown loading time signal $f(t)$, for which arbitrary temporal variability is allowed. To this end, $f(t)$ is parameterized as:

$$f(t) = \sum_{i=1}^{n_f} f_i \varphi_i(t) = \mathbf{f}\boldsymbol{\varphi}^T(t), \tag{12}$$

where $\varphi_i(t)$ and f_i denote the i-th shape function and discretized excitation parameter, respectively; $\mathbf{f}$ is the vector of force parameters f_i, and $\boldsymbol{\varphi}$ is the vector of shape functions $\varphi_i(t)$; and n_f is the total number of parameters; we use quadratic shape functions as $\varphi_i(t)$ (Figure 3).

3. PDE-constrained optimization

This section presents a mathematical modeling approach for identification of the control parameters that minimize the objective functional (11) subject to the governing wave physics (1)–(10). To tackle such a PDE-constrained minimization problem with a large set of control parameters, an augmented functional is constructed via the side-imposition of the governing wave physics, using Lagrange multipliers, into the objective functional. The first-order optimality conditions of the augmented functional lead to a triplet of state, adjoint, and control problems.

3.1. Augmented functional

An augmented functional is built by side-imposing the governing PDEs (1), (2), and (3), as well as the associated conditions (6) and (7) into the objective functional (11), by means of Lagrange multipliers[4] ($\lambda_{u_a}(x,t)$, $\lambda_{u_b}(x,t)$, $\lambda_w(x,t)$, $\lambda_0(t)$, and $\lambda_L(t)$) as the following:

$$\begin{aligned}\mathcal{A} = \Bigg\{ & \frac{1}{\int_{\Omega_p}\int_0^T \rho_f (\frac{\partial w}{\partial t})^2 \mathrm{d}t\mathrm{d}x} \\ & + \int_{\Omega\setminus\Omega_p}\int_0^T \lambda_{u_a}\left[\frac{\partial}{\partial x}\left((\lambda+2\mu)\frac{\partial u_a}{\partial x}\right) - \rho\frac{\partial^2 u_a}{\partial t^2}\right]\mathrm{d}t\mathrm{d}x\end{aligned}$$

$$
\begin{aligned}
&+\int_{\Omega_p}\int_0^T \lambda_{u_\mathrm{b}}\left[\frac{\partial}{\partial x}\left((\lambda+2\mu+\alpha^2 Q)\frac{\partial u_\mathrm{b}}{\partial x}+\alpha Q\frac{\partial w}{\partial x}\right)\right.\\
&\qquad\left.-\rho\frac{\partial^2 u_\mathrm{b}}{\partial t^2}-\rho_f\frac{\partial^2 w}{\partial t^2}\right]\mathrm{d}t\mathrm{d}x\\
&+\int_{\Omega_p}\int_0^T \lambda_w\left[\frac{\partial}{\partial x}\left(\alpha Q\frac{\partial u_\mathrm{b}}{\partial x}+Q\frac{\partial w}{\partial x}\right)-\frac{1}{k}\frac{\partial w}{\partial t}-\rho_f\frac{\partial^2 u_\mathrm{b}}{\partial t^2}-\frac{\rho_f}{n}\frac{\partial^2 w}{\partial t^2}\right]\mathrm{d}t\mathrm{d}x\\
&+\int_0^T \lambda_0(t)\left[(\lambda(0)+2\mu(0))\frac{\partial u_\mathrm{a}}{\partial x}(0,t)+f(t)\right]\mathrm{d}t\\
&+\int_0^T \lambda_L(t)\left[(\lambda(L)+2\mu(L))\left\{\frac{\partial u_\mathrm{a}}{\partial x}(L,t)+\frac{1}{c}\frac{\partial u_\mathrm{a}}{\partial t}(L,t)\right\}\right]\mathrm{d}t\Bigg\}. \qquad (13)
\end{aligned}
$$

In the augmented functional (13), the zero initial value conditions and the interface conditions (8)–(10) are implicitly imposed. The dimensions of the Lagrange multipliers $\lambda_{u_\mathrm{a}}, \lambda_{u_\mathrm{b}}, \lambda_w, \lambda_0$, and λ_L are all identical to each other.

3.2. The first-order optimality conditions

To arrive at the minimum of $\mathcal{A}$, the variations of $\mathcal{A}$ with respect to the state variables (u_a, u_b, and w), the Lagrange multipliers (λ_{u_a}, λ_{u_b}, λ_w, λ_0, and λ_L), and the control variable $\xi = f_i$ – the value of a discretized force parameter used for the temporal approximation of a loading signal as in (12) – should vanish as the first-order optimality conditions. That is,

$$
\left\{\begin{array}{l}\delta_{\lambda_{u_\mathrm{a}}}\mathcal{A}=0\\ \delta_{\lambda_{u_\mathrm{b}}}\mathcal{A}=0\\ \delta_{\lambda_w}\mathcal{A}=0\\ \delta_{\lambda_0}\mathcal{A}=0\\ \delta_{\lambda_L}\mathcal{A}=0\end{array}\right\}\ \text{: yields the state initial BVP,}
$$

$$
\left\{\begin{array}{l}\delta_{u_\mathrm{a}}\mathcal{A}=0\\ \delta_{u_\mathrm{b}}\mathcal{A}=0\\ \delta_{w}\mathcal{A}=0\end{array}\right\}\ \text{: yields the adjoint final BVP,}
$$

$$
\delta_\xi\mathcal{A}=0\quad\text{: yields the control problem.}
$$

3.2.1. The first optimality condition

As the first optimality condition, the variation of $\mathcal{A}$ with respect to the Lagrange multipliers λ_{u_a}, λ_{u_b}, λ_w, λ_0, and λ_L should vanish for arbitrary variations $\delta\lambda_{u_\mathrm{a}}$, $\delta\lambda_{u_\mathrm{b}}$, $\delta\lambda_w$, $\delta\lambda_0$, and $\delta\lambda_L$. To this end, one must satisfy *the state problem*, which is identical to the governing wave physics described in (1)–(10).

3.2.2. The second optimality condition

The second optimality condition requires the variation of $\mathcal{A}$ with respect to the state variables (u_a, u_b, and w) to vanish, i.e. $\delta_{u_\mathrm{a}}\mathcal{A}+\delta_{u_\mathrm{b}}\mathcal{A}+\delta_w\mathcal{A}=0$, for arbitrary variations δu_a, δu_b, and δw. Such a vanishing variation recovers the following adjoint problem (for brevity, the explicit derivation of the adjoint problem is not shown in this paper):

The adjoint problem:

$$\frac{\partial}{\partial x}\left((\lambda+2\mu)\frac{\partial \lambda_{u_{\mathrm{a}}}}{\partial x}\right)-\rho\frac{\partial^2\lambda_{u_{\mathrm{a}}}}{\partial t^2}=0,\quad x\in\Omega\setminus\Omega_p,\quad t\in[0,T), \tag{14}$$

$$\frac{\partial}{\partial x}\left((\lambda+2\mu+\alpha^2Q)\frac{\partial \lambda_{u_{\mathrm{b}}}}{\partial x}+(\alpha Q)\frac{\partial \lambda_w}{\partial x}\right)-\rho\frac{\partial^2\lambda_{u_{\mathrm{b}}}}{\partial t^2}-\rho_f\frac{\partial^2\lambda_w}{\partial t^2}=0,$$
$$x\in\Omega_p,\quad t\in[0,T), \tag{15}$$

$$\frac{\partial}{\partial x}\left(\alpha Q\frac{\partial \lambda_{u_{\mathrm{b}}}}{\partial x}+Q\frac{\partial \lambda_w}{\partial x}\right)+\frac{1}{k}\frac{\partial \lambda_w}{\partial t}-\rho_f\frac{\partial^2\lambda_{u_{\mathrm{b}}}}{\partial t^2}-\frac{\rho_f}{n}\frac{\partial^2\lambda_w}{\partial t^2}-\mathcal{E}\rho_f\frac{\partial^2 w}{\partial t^2}=0,$$
$$x\in\Omega_p,\quad t\in[0,T), \tag{16}$$

where the coefficient $\mathcal{E}$ is defined as the following:

$$\mathcal{E}=\frac{-2}{\left(\int_{\Omega_p}\int_0^T\rho_f[\frac{\partial w}{\partial t}]^2\mathrm{d}t\mathrm{d}x\right)^2}. \tag{17}$$

The adjoint problem is subject to the following final-value conditions:

$$\lambda_{u_{\mathrm{a}}}(x,T)=0,\quad \frac{\partial \lambda_{u_{\mathrm{a}}}}{\partial t}(x,T)=0,\quad x\in\Omega\setminus\Omega_p, \tag{18a}$$

$$\frac{\partial \lambda_{u_{\mathrm{b}}}}{\partial t}(x,T)=\frac{-\mathcal{E}\rho_f}{\rho_f-\frac{\rho}{n}}\frac{\partial w}{\partial t}(x,T),\quad x\in\Omega_p, \tag{18b}$$

$$\frac{\partial \lambda_w}{\partial t}(x,T)=\frac{\rho\mathcal{E}\rho_f}{\rho_f\left(\rho_f-\frac{\rho}{n}\right)}\frac{\partial w}{\partial t}(x,T),\quad x\in\Omega_p, \tag{18c}$$

as well as the following boundary and truncation interface conditions:

$$\left(\lambda(0)+2\mu(0)\right)\frac{\partial \lambda_{u_{\mathrm{a}}}}{\partial x}(0,t)=0,\quad t\in[0,T), \tag{19}$$

$$\frac{\partial \lambda_{u_{\mathrm{a}}}}{\partial x}(L,t)-\frac{1}{c(L)}\frac{\partial \lambda_{u_{\mathrm{a}}}(t)}{\partial t}(L,t)=0,\quad t\in[0,T). \tag{20}$$

Similarly to the state problem, the adjoint PDE (14) is coupled with the other adjoint PDEs (15) and (16) via the following conditions at the interfaces between the poroelastic layers and the elastic solid layers:

$$\begin{aligned}\lambda_{u_{\mathrm{a}}}\big|_{x_i^-}&=\lambda_{u_{\mathrm{b}}}\big|_{x_i^+},\quad i=p,\\ \lambda_{u_{\mathrm{a}}}\big|_{x_i^+}&=\lambda_{u_{\mathrm{b}}}\big|_{x_i^-},\quad i=p+N_{\mathrm{pls}},\end{aligned} \tag{21a}$$

$$\begin{aligned}(\lambda+2\mu)\frac{\partial \lambda_{u_{\mathrm{a}}}}{\partial x}\Big|_{x_i^-}&=(\lambda+2\mu+\alpha^2Q)\frac{\partial \lambda_{u_{\mathrm{b}}}}{\partial x}+(\alpha Q)\frac{\partial \lambda_w}{\partial x}\Big|_{x_i^+},\quad i=p,\\ (\lambda+2\mu)\frac{\partial \lambda_{u_{\mathrm{a}}}}{\partial x}\Big|_{x_i^+}&=(\lambda+2\mu+\alpha^2Q)\frac{\partial \lambda_{u_{\mathrm{b}}}}{\partial x}+(\alpha Q)\frac{\partial \lambda_w}{\partial x}\Big|_{x_i^-},\quad i=p+N_{\mathrm{pls}},\end{aligned} \tag{21b}$$

$$\lambda_w\big|_{x_i}=0,\quad i=p \text{ and } p+N_{\mathrm{pls}}. \tag{21c}$$

Equations (21a), (21b), and (21c) replicate, respectively, the rock displacement-continuity (8a), the total stress-continuity (8b), and the zero relative-fluid-displacement (8c) conditions of the state problem.

In addition, for a multi-layered system, the adjoint problem is subject to the following continuity conditions at the interfaces between the mutually-neighboring elastic solid layers (i.e. the interface indices: $i = 2, \ldots, (p-1)$ and $(p + N_{\text{pls}} + 1), \ldots, N_{\text{ls}}$):

$$\lambda_{u_{\text{a}}}\Big|_{x_i^-} = \lambda_{u_{\text{a}}}\Big|_{x_i^+}, \tag{22a}$$

$$(\lambda + 2\mu)\frac{\partial \lambda_{u_{\text{a}}}}{\partial x}\Big|_{x_i^-} = (\lambda + 2\mu)\frac{\partial \lambda_{u_{\text{a}}}}{\partial x}\Big|_{x_i^+}, \tag{22b}$$

as well as the following continuity conditions at the interfaces between the mutually-adjacent poroelastic layers (i.e. the interface indices: $i = (p+1), \ldots, (p + N_{\text{pls}} - 1)$):

$$\lambda_{u_{\text{b}}}\Big|_{x_i^-} = \lambda_{u_{\text{b}}}\Big|_{x_i^+}, \tag{23a}$$

$$\lambda_{w}\Big|_{x_i^-} = \lambda_{w}\Big|_{x_i^+}, \tag{23b}$$

$$(\lambda + 2\mu + \alpha^2 Q)\frac{\partial \lambda_{u_{\text{b}}}}{\partial x} + \alpha Q\frac{\partial \lambda_{w}}{\partial x}\Big|_{x_i^-} = (\lambda + 2\mu + \alpha^2 Q)\frac{\partial \lambda_{u_{\text{b}}}}{\partial x} + \alpha Q\frac{\partial \lambda_{w}}{\partial x}\Big|_{x_i^+}, \tag{23c}$$

$$\alpha Q\frac{\partial \lambda_{u_{\text{b}}}}{\partial x} + Q\frac{\partial \lambda_{w}}{\partial x}\Big|_{x_i^-} = \alpha Q\frac{\partial \lambda_{u_{\text{b}}}}{\partial x} + Q\frac{\partial \lambda_{w}}{\partial x}\Big|_{x_i^+}. \tag{23d}$$

Equations (22a) and (22b) replicate the continuity conditions of the displacement and stress between elastic solid layers, respectively, shown in (9a) and (9b). Equations (23a)–(23d) replicate the continuity conditions of the displacement of rock matrix, the relative displacement of pore fluid, the total stress, and the pore pressure between poroelastic layers, respectively, shown in (10a)–(10d).

It should be noted that the governing differential operators of the adjoint PDEs are identical to those of the state PDEs, while the adjoint problem differs from the state problem with respect to the following points. First, the body force term $\mathcal{E}\rho_f \frac{\partial^2 w}{\partial t^2}$ in (16), as well as the final value conditions (**??**) drive the adjoint problem, whereas the state problem is driven by the surface excitation. Second, the adjoint problem is a final BVP such that the sign of the time derivative in the truncation condition (20) of the adjoint problem is reversed compared with that of the truncation condition (7) of the state problem (an initial BVP).

3.2.3. The third optimality condition

We consider the vanishing variation of the augmented functional $\mathcal{A}$ with respect to a scalar variable ξ, tantamount to a parameter f_i – a discretized force parameter of the force function $f(t)$ (see (12)). To this end, $\delta_\xi \mathcal{A} = \frac{\partial \mathcal{A}}{\partial \xi}$ is required to vanish. Such a vanishing variation condition leads to the following control equation (for brevity, the explicit derivation of the control problem is not shown in this paper):

The control problem:

$$\delta_\xi \mathcal{A}(= \nabla_\xi \mathcal{A}) = \int_0^T \lambda_{u_{\text{a}}}(0,t)\frac{\partial f(t)}{\partial \xi}\mathrm{d}t = 0. \tag{24}$$

It should be noted that $\delta_\xi \mathcal{A} (= \nabla_\xi \mathcal{A})$ is equivalent to the gradient of the objective functional $\nabla_\xi \mathcal{L}$, since the side-imposed constraints to the augmented functional $\mathcal{A}$ vanish at the stationary point owing to the satisfaction of the state problem. To obtain the excitation parameters, we use a gradient-based minimization process and $\int_0^T \lambda_{u_a}(0,t)\frac{\partial f(t)}{\partial \xi}\mathrm{d}t$, in the control equation (24), as the reduced gradient.

4. Numerical implementation

Satisfaction of the first-order optimality conditions, upon discretization, gives rise to a Karush–Kuhn–Tucker (KKT) system.[84,85] Stationarity can be achieved by solving the state, adjoint, and control problems either as a fully-coupled problem (a full-space solution approach), or via a reduced-space approach. Since the computational cost associated with a full-space approach is rather significant,[86] here, we solve the KKT system by projecting the state and adjoint variables into the space of the control variables. Such a reduced-space solution approach entails the following steps: (a) first, the state problem is solved for an initial guess of the excitation; (b) the adjoint problem is then solved using, as driver, the acceleration field of the pore-fluid motion $w(x,t)$ of the state problem (per (16)); (c) finally, updates to the control parameters, defining the trial form of the excitation, are obtained via a gradient-based scheme that uses the control equation (24) as the reduced gradient: at each iteration, the control equation provides the search-direction for the parameter updating. Here, a conjugate-gradient(CG) scheme [87,88] is used with an inexact line-search method. The numerical optimizer repeats the above procedure, (a)–(c), to iteratively solve for the control parameters that satisfy the vanishing control equation (the detailed procedure is described in Algorithm 1). The details of the numerical implementation of the state and adjoint solvers are described as follows.

Algorithm 1 Optimization algorithm

Set TOL=10^{-8}, $\alpha = 0.9$ and $\beta = 1.1$
Set $k = 0$ and Initial Force Parameters $\mathbf{f}_{(0)}$
Compute $\mathcal{L}_{(k)}$
while ($e >$ TOL) **do**
    Solve the Discrete Form of the State Problem, (40), and Save the State Variables
    Solve the Discrete Form of the Adjoint Problem, (41), and Save the Adjoint Variables
    Compute the Search-Direction $\mathbf{g}$ Using the Reduced Gradient (42) and the Conjugate-Gradient Scheme
    Reduce the Step Length $\theta_{(k)}$ if the Updating of the Control Parameters with $\theta_{(k)}\mathbf{g}$ does not Sufficiently Decrease the Value of $\mathcal{L}$:
    while ($\mathcal{L}(\mathbf{f}_{(k)} + \theta_{(k)}\mathbf{g}) > \mathcal{L}(\mathbf{f}_{(k)} - \frac{1}{2}\theta_{(k)}\nabla\mathcal{L}(\mathbf{f}_{(k)}))$ **do**
        $\theta_{(k)} \leftarrow \alpha\theta_{(k)}$
    end while
    Update Excitation Parameters, as $\mathbf{f}_{(k+1)} = \mathbf{f}_{(k)} + \mathbf{g}\theta_{(k)}$, and Compute $\mathcal{L}_{(k+1)}$
    Compute the Iterative Norm, $e = \frac{|\mathcal{L}_{(k+1)} - \mathcal{L}_{(k)}|}{|\mathcal{L}_{(k)}|}$:
    $\theta_{(k+1)} \leftarrow \beta\theta_{(k)}$ and $k \leftarrow k + 1$
end while

4.1. State problem semi-discrete form

This subsection presents the $u-w$ mixed finite element formulation [73,75,76,89] used for tackling the governing wave equations (1)–(3). The elastic wave equation (1) is multiplied by a test function $s(x)$ and integrated over the elastic solid media ($x \in (x_1, x_p)$) that is situated atop the poroelastic layers. Then, integration by parts with respect to x gives rise to the weak form:

$$\int_{x_1}^{x_p} \frac{\partial s}{\partial x}\left((\lambda+2\mu)\frac{\partial u_{\mathrm{a}}}{\partial x}\right)\mathrm{d}x + \int_{x_1}^{x_p} s\rho\frac{\partial^2 u_{\mathrm{a}}}{\partial t^2}\mathrm{d}x = s(\lambda+2\mu)\frac{\partial u_{\mathrm{a}}}{\partial x}\bigg|_{x_p} - sf(t)\big|_{x_1}. \tag{25}$$

Similarly, for the elastic solid media ($x \in (x_{p+N_{\mathrm{pls}}}, L)$) that is located below the poroelastic layers, there arises the following weak form:

$$\begin{aligned}\int_{x_{p+N_{\mathrm{pls}}}}^{L} \frac{\partial s}{\partial x}\left((\lambda+2\mu)\frac{\partial u_{\mathrm{a}}}{\partial x}\right)\mathrm{d}x + \int_{x_{p+N_{\mathrm{pls}}}}^{L} s\rho\frac{\partial^2 u_{\mathrm{a}}}{\partial t^2}\mathrm{d}x \\ = -s\frac{(\lambda+2\mu)}{c}\frac{\partial u_{\mathrm{a}}}{\partial t}\bigg|_{x=L} - s(\lambda+2\mu)\frac{\partial u_{\mathrm{a}}}{\partial x}\bigg|_{x_{p+N_{\mathrm{pls}}}}.\end{aligned} \tag{26}$$

Similarly, by using the test function $s(x)$, one obtains the weak form of the first equation (2) for the poroelastic layers ($x \in (x_p, x_{p+N_{\mathrm{pls}}})$):

$$\begin{aligned}&\int_{x_p}^{x_{p+N_{\mathrm{pls}}}} \frac{\partial s}{\partial x}\left((\lambda+2\mu+\alpha^2 Q)\frac{\partial u_{\mathrm{b}}}{\partial x} + (\alpha Q)\frac{\partial w}{\partial x}\right)\mathrm{d}x \\ &\quad + \int_{x_p}^{x_{p+N_{\mathrm{pls}}}} s\left(\rho\frac{\partial^2 u_{\mathrm{b}}}{\partial t^2} + \rho_f\frac{\partial^2 w}{\partial t^2}\right)\mathrm{d}x \\ &\quad = s\left((\lambda+2\mu+\alpha^2 Q)\frac{\partial u_{\mathrm{b}}}{\partial x} + (\alpha Q)\frac{\partial w}{\partial x}\right)\bigg|_{x_{p+N_{\mathrm{pls}}}} \\ &\quad - s\left((\lambda+2\mu+\alpha^2 Q)\frac{\partial u_{\mathrm{b}}}{\partial x} + (\alpha Q)\frac{\partial w}{\partial x}\right)\bigg|_{x_p}.\end{aligned} \tag{27}$$

We, in turn, obtain the weak form of the second equation (3) for the poroelastic layers ($x \in (x_p, x_{p+N_{\mathrm{pls}}})$) by using another test function $v(x)$ as follows:

$$\begin{aligned}&\int_{x_p}^{x_{p+N_{\mathrm{pls}}}} \frac{\partial v}{\partial x}(\alpha Q)\frac{\partial u_{\mathrm{b}}}{\partial x}\mathrm{d}x + \int_{x_p}^{x_{p+N_{\mathrm{pls}}}} \frac{\partial v}{\partial x}Q\frac{\partial w}{\partial x}\mathrm{d}x \\ &\quad + \int_{x_p}^{x_{p+N_{\mathrm{pls}}}} v\left[\frac{1}{k}\frac{\partial w}{\partial t} + \rho_f\frac{\partial^2 u_{\mathrm{b}}}{\partial t^2} + \frac{\rho_f}{n}\frac{\partial^2 w}{\partial t^2}\right]\mathrm{d}x = 0.\end{aligned} \tag{28}$$

We introduce the spatial approximation of the test functions $s(x)$ and $v(x)$, as well as the trial functions $u(x,t)$ and $w(x,t)$ as:

$$\begin{aligned}&s(x) = \mathbf{s}^T\boldsymbol{\Phi}(x), \quad v(x) = \mathbf{v}^T\boldsymbol{\Psi}(x), \\ &u(x,t) = \boldsymbol{\Phi}^T(x)\mathbf{u}(t), \quad w(x,t) = \boldsymbol{\Psi}^T(x)\mathbf{w}(t),\end{aligned} \tag{29}$$

where $\mathbf{s}$ and $\mathbf{v}$ denote the vectors of nodal solutions of $s(x)$ and $v(x)$, respectively; $\mathbf{u}(t)$ and $\mathbf{w}(t)$ denote the vectors of nodal solutions of $u(x,t)$ and $w(x,t)$ at time t, respectively. Here, it should be noted that, by virtue of the continuity conditions (8a), $u_{\mathrm{a}}(x,t)$ and $u_{\mathrm{b}}(x,t)$ are merged into $u(x,t)$. $\mathbf{\Phi}(x)$ and $\mathbf{\Psi}(x)$ are the vectors of shape functions for the spatial approximation of the trial and test functions. Owing to the finite element approximation, the summation of the weak forms (25), (26), and (27) yields the following time-dependent semi-discrete form:

$$\mathbf{K}_{uu}\mathbf{u} + \mathbf{K}_{uw}\mathbf{w} + \mathbf{C}_{uu}\frac{\partial \mathbf{u}}{\partial t} + \mathbf{M}_{uu}\frac{\partial^2 \mathbf{u}}{\partial t^2} + \mathbf{M}_{uw}\frac{\partial^2 \mathbf{w}}{\partial t^2} = \mathbf{f}_u, \tag{30}$$

where the specific forms of the matrices are:

$$\begin{aligned}
\mathbf{K}_{uu} &= \int_{\Omega\setminus\Omega_p} (\lambda + 2\mu)\frac{\partial \mathbf{\Phi}}{\partial x}\frac{\partial \mathbf{\Phi}^T}{\partial x}\mathrm{d}x + \int_{\Omega_p} (\lambda + 2\mu + \alpha^2 Q)\frac{\partial \mathbf{\Phi}}{\partial x}\frac{\partial \mathbf{\Phi}^T}{\partial x}\mathrm{d}x,\\
\mathbf{K}_{uw} &= \int_{\Omega_p} (\alpha Q)\frac{\partial \mathbf{\Phi}}{\partial x}\frac{\partial \mathbf{\Psi}^T}{\partial x}\mathrm{d}x, \quad \mathbf{C}_{uu} = \frac{(\lambda + 2\mu)}{c}\mathbf{\Phi}(L)\mathbf{\Phi}^T(L),\\
\mathbf{M}_{uu} &= \int_{\Omega} \rho \mathbf{\Phi}\mathbf{\Phi}^T \mathrm{d}x, \quad \mathbf{M}_{uw} = \int_{\Omega_p} \rho_f \mathbf{\Phi}\mathbf{\Psi}^T \mathrm{d}x,\\
\mathbf{f}_u &= \mathbf{\Phi}(0) f(t).
\end{aligned} \tag{31}$$

Similarly, the weak form (28) changes to the following time-dependent discrete form:

$$\mathbf{K}_{wu}\mathbf{u} + \mathbf{K}_{ww}\mathbf{w} + \mathbf{C}_{ww}\frac{\partial \mathbf{w}}{\partial t} + \mathbf{M}_{wu}\frac{\partial^2 \mathbf{u}}{\partial t^2} + \mathbf{M}_{ww}\frac{\partial^2 \mathbf{w}}{\partial t^2} = 0, \tag{32}$$

where the specific forms of the matrices are:

$$\begin{aligned}
\mathbf{K}_{wu} &= \int_{\Omega_p} (\alpha Q)\frac{\partial \mathbf{\Psi}}{\partial x}\frac{\partial \mathbf{\Phi}^T}{\partial x}\mathrm{d}x, \quad \mathbf{K}_{ww} = \int_{\Omega_p} Q\frac{\partial \mathbf{\Psi}}{\partial x}\frac{\partial \mathbf{\Psi}^T}{\partial x}\mathrm{d}x,\\
\mathbf{C}_{ww} &= \int_{\Omega_p} \frac{1}{k}\mathbf{\Psi}\mathbf{\Psi}^T \mathrm{d}x,\\
\mathbf{M}_{wu} &= \int_{\Omega_p} \rho_f \mathbf{\Psi}\mathbf{\Phi}^T \mathrm{d}x, \quad \mathbf{M}_{ww} = \int_{\Omega_p} \frac{\rho_f}{n}\mathbf{\Psi}\mathbf{\Psi}^T \mathrm{d}x.
\end{aligned} \tag{33}$$

Then, (30) and (32) lead to the following time-dependent discrete form of the state problem:

$$\mathbf{M}\frac{\partial^2 \mathbf{q}(t)}{\partial t^2} + \mathbf{C}\frac{\partial \mathbf{q}(t)}{\partial t} + \mathbf{K}\,\mathbf{q}(t) = \mathbf{f}_{\mathrm{st}}, \tag{34}$$

where

$$\begin{aligned}
\mathbf{M} &= \begin{bmatrix} \mathbf{M}_{uu} & \mathbf{M}_{uw} \\ \mathbf{M}_{wu} & \mathbf{M}_{ww} \end{bmatrix}, \quad \mathbf{C} = \begin{bmatrix} \mathbf{C}_{uu} & \mathbf{0} \\ \mathbf{0} & \mathbf{C}_{ww} \end{bmatrix},\\
\mathbf{K} &= \begin{bmatrix} \mathbf{K}_{uu} & \mathbf{K}_{uw} \\ \mathbf{K}_{wu} & \mathbf{K}_{ww} \end{bmatrix}, \quad \mathbf{q}(t) = \begin{bmatrix} \mathbf{u}(t) \\ \mathbf{w}(t) \end{bmatrix}, \quad \mathbf{f}_{\mathrm{st}} = \begin{bmatrix} \mathbf{f}_u \\ \mathbf{0} \end{bmatrix}.
\end{aligned} \tag{35}$$

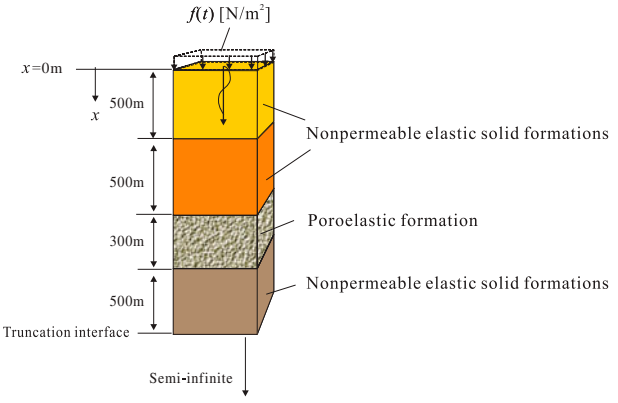

Figure 4. Four layered semi-infinite coupled-poroelastic-elastic-layers system truncated at depth $x = 1800$ m.

4.2. Adjoint problem semi-discrete form

Similarly to the state problem, by using the test functions $s(x)$ and $v(x)$, the weak forms of the adjoint PDEs (14) to (16) are built. We then introduce the approximation of the test functions $s(x)$ and $v(x)$ shown in (29), as well as the adjoint solutions $\lambda_u(x,t)$ and $\lambda_w(x,t)$ as:

$$\lambda_u(x,t) = \mathbf{\Phi}^T(x)\boldsymbol{\lambda}_u(t), \quad \lambda_w(x,t) = \mathbf{\Psi}^T(x)\boldsymbol{\lambda}_w(t), \tag{36}$$

where $\boldsymbol{\lambda}_u(t)$ and $\boldsymbol{\lambda}_w(t)$ denotes the vector of the nodal solutions of $\lambda_u(x,t)$ and $\lambda_w(x,t)$, respectively. Owing to the continuity condition (21a), $\lambda_{u_a}(x,t)$ and $\lambda_{u_b}(x,t)$ are merged into $\lambda_u(x,t)$. Then, similarly to the state problem, the weak forms of the adjoint problem change to the following time-dependent discrete form of the adjoint problem:

$$\mathbf{M}\frac{\partial^2 \mathbf{r}(t)}{\partial t^2} - \mathbf{C}\frac{\partial \mathbf{r}(t)}{\partial t} + \mathbf{K}\,\mathbf{r}(t) = \mathbf{f}_{\text{adj}}, \tag{37}$$

where the adjoint solution vector $\boldsymbol{\lambda}(t)$ is defined as the following:

$$\mathbf{r}(t) = \begin{bmatrix} \boldsymbol{\lambda}_u(t) \\ \boldsymbol{\lambda}_w(t) \end{bmatrix}. \tag{38}$$

The specific forms of the matrices $\mathbf{M}$, $\mathbf{C}$, and $\mathbf{K}$ are identical to those for the state problem already shown in (35); the force vector $\mathbf{f}_{\text{adj}}$ is defined as:

$$\mathbf{f}_{\text{adj}} = -\begin{bmatrix} \mathbf{0} \\ \mathcal{E}\int_{\Omega_p} \rho_f \mathbf{\Psi}\mathbf{\Psi}^T \mathrm{d}x \frac{\partial^2 \mathbf{w}}{\partial t^2} \end{bmatrix}, \tag{39}$$

where the state solution vector $\mathbf{w}$ is obtained by solving (34).

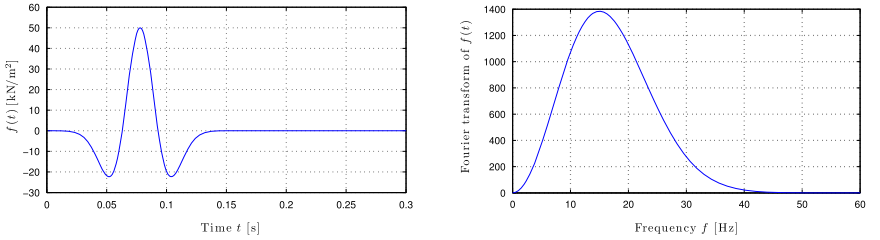

(a) The Ricker pulse time signal

(b) The frequency spectrum of the Ricker pulse signal

Figure 5. The Ricker pulse signal with a central frequency of $f = \frac{\omega_r}{2\pi} = 15$ Hz.

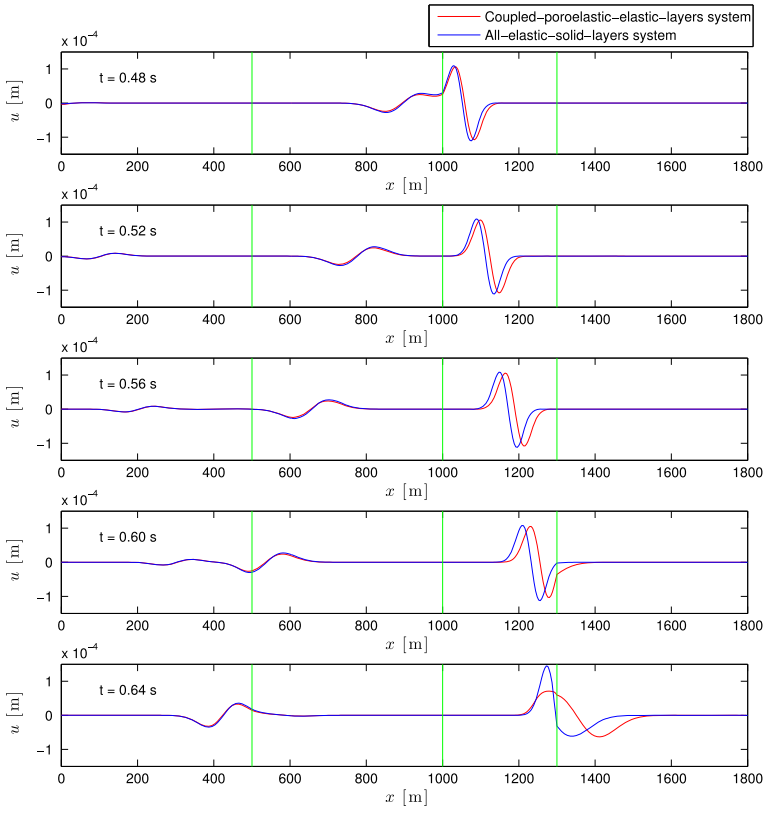

Figure 6. Comparison of the numerical solution of $u(x, t)$ of the coupled-poroelastic-elastic-layers system (using $n = 0.3$ and $\alpha = 0.667$) with that of the all-elastic-solid-layers system, 0.48 s $\leq t \leq$ 0.64 s. The green vertical lines indicate the interfaces between the layers.

4.3. *Time integration and evaluation of the gradient*

We resolve the semi-discrete forms (34) and (37) by using the implicit Newmark time integration [90] with the average acceleration scheme (unconditionally stable). Accordingly, the discrete solutions of the state and adjoint problems are obtained by solving the following systems of equations:

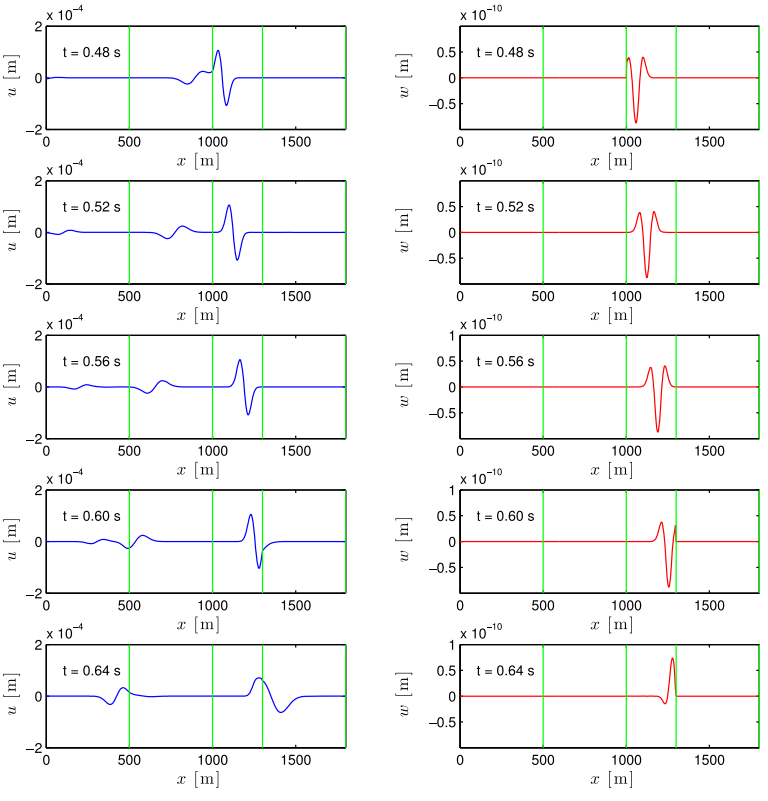

Figure 7. The numerical solution of $u(x,t)$ and $w(x,t)$ of the coupled-poroelastic-elastic-layers system employing $n = 0.3$ and $\alpha = 0.667$, $0.48\text{ s} \le t \le 0.64\text{ s}$.

$$\begin{aligned}
&\left[\mathbf{M} + \mathbf{C}\frac{\Delta t}{2} + \mathbf{K}\frac{(\Delta t)^2}{4}\right]\frac{\partial^2 \mathbf{q}_{(j+1)}}{\partial t^2} \\
&\qquad = \mathbf{f}_{\mathrm{st}(j+1)} - \mathbf{C}\left[\frac{\partial \mathbf{q}_{(j)}}{\partial t} + \frac{\partial^2 \mathbf{q}_{(j)}}{\partial t^2}\frac{\Delta t}{2}\right] \\
&\qquad\quad - \mathbf{K}\left[\mathbf{q}_{(j)} + \frac{\partial \mathbf{q}_{(j)}}{\partial t}(\Delta t) + \frac{\partial^2 \mathbf{q}_{(j)}}{\partial t^2}\frac{(\Delta t)^2}{4}\right], \qquad (40)\\
&\left[\mathbf{M} + \mathbf{C}\frac{\Delta t}{2} + \mathbf{K}\frac{(\Delta t)^2}{4}\right]\frac{\partial^2 \mathbf{r}_{(j)}}{\partial t^2} \\
&\qquad = \mathbf{f}_{\mathrm{adj}_{(j)}} + \mathbf{C}\left[\frac{\partial \mathbf{r}_{(j+1)}}{\partial t} - \frac{\partial^2 \mathbf{r}_{(j+1)}}{\partial t^2}\frac{\Delta t}{2}\right] \\
&\qquad\quad - \mathbf{K}\left[\mathbf{r}_{(j+1)} - \frac{\partial \mathbf{r}_{(j+1)}}{\partial t}\Delta t + \frac{\partial^2 \mathbf{r}_{(j+1)}}{\partial t^2}\frac{(\Delta t)^2}{4}\right], \qquad (41)
\end{aligned}$$

where Δt is the time step; (j) and $(j+1)$ denote evaluation of the nodal vectors at the j-th and $(j+1)$-th time steps; and the time-line of the evaluation of solution in (41) is reversed with respect to that of (40). It should be remarked that the system matrix in (40) is identical

to that in (41) such that only one system matrix inversion is required for addressing both the state and adjoint problems.

By using the discrete adjoint solution, the reduced gradient is evaluated as follows:

$$\nabla_{(\xi=f_i)}\mathcal{L} = \int_0^T \lambda_{u_a}(0,t)\frac{\partial f(t)}{\partial f_i}\mathrm{d}t = \int_0^T \mathbf{\Phi}^T(0)\boldsymbol{\lambda}_u(t)\varphi_i(t)\mathrm{d}t. \tag{42}$$

Equation (42) provides the search-direction information to the numerical optimizer for updating the values of the control parameters.

4.3.1. Verification of the inverse modeling

We have thus far discussed the numerical implementation for solving the state and adjoint problems, as well as evaluating the gradient of the objective functional. We verified the derivation and implementation of the state, adjoint, and control problems by comparing the values of the components of the gradient, computed by (42), with their counterpart obtained by the finite difference scheme as:

$$\nabla_{f_i}\mathcal{L} = \frac{\mathcal{L}\big|_{f_i+\Delta f_i} - \mathcal{L}\big|_{f_i-\Delta f_i}}{2\Delta f_i}, \tag{43}$$

where Δf_i denotes an incremental value of f_i used for the finite difference scheme. The comparison shows excellent agreement. We conduct the numerical experiments using the numerical optimizer, implemented per the above discussion.

5. Numerical results

In this section, we first present the numerical solution of the forward problem for a multi-layered system, where the wave equations for the poroelastic layers and the elastic wave equation are coupled with each other. Secondly, it is shown that the presented numerical optimizer leads to the optimal loading time signal of a wave source that can maximize the kinetic energy in terms of the relative displacement of pore fluid, i.e. $w(x,t)$. The dominant frequencies of the optimized time signals recover the amplification frequencies of the pore-fluid wave motion within a target poroelastic layer, which can be also numerically obtained by a frequency sweep.

5.1. Forward wave solution

This section presents the forward numerical solution of the wave response within a coupled-poroelastic-elastic-layers system, where the wave equations for the poroelastic layers are coupled with the elastic wave equation. We obtain the numerical solution of the wave responses of the coupled-poroelastic-elastic-layers system, shown in Figure 4, for which the material parameters are described in Table 1. We use realistic values – corresponding to a typical hydrocarbon reservoir rock formation – of the material parameters of the poroelastic layer. Linear elements are used for the approximation of both

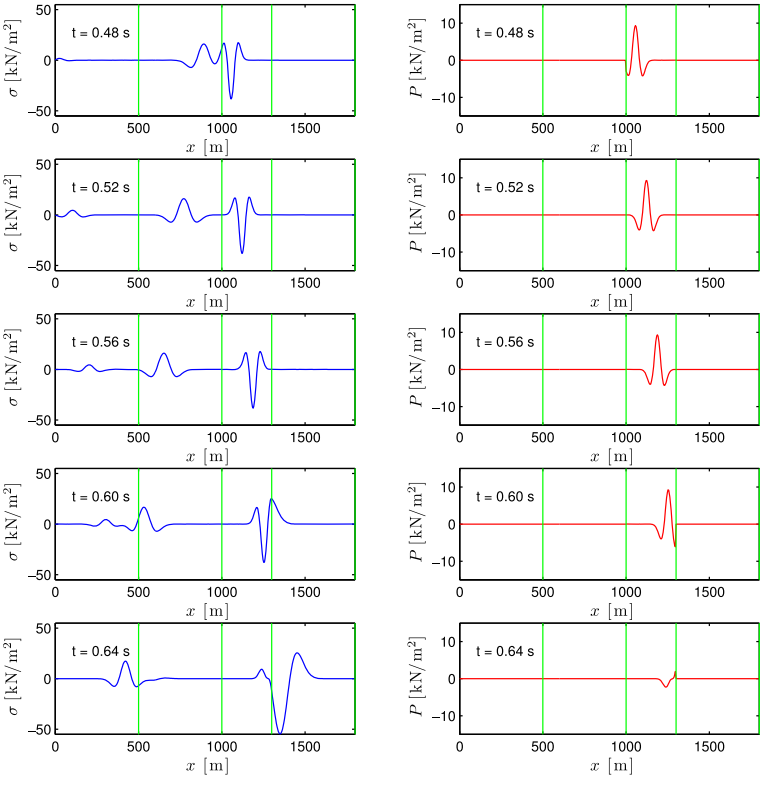

Figure 8. The numerical solution of $\sigma(x,t)$ and $P(x,t)$ of the coupled-poroelastic-elastic-layers system employing $n = 0.3$ and $\alpha = 0.667$, 0.48 s $\leq t \leq$ 0.64 s; $P(x,t)$ is positive for compression.

$u(x,t)$ and $w(x,t)$, with an element size of 4 m. The total observation duration is $T = 10$ s, and the time step is $\Delta t = 0.001$ s. The modified Ricker pulse loading, described in (44) and Figure 5, is used with a central frequency of $f = 15$ Hz (Figure 5(b)).

$$f(t) = -50 \times \frac{(0.25\eta^2 - 0.5)e^{(-0.25\eta^2)} - 13.0e^{-13.5}}{0.5 + 13.0e^{-13.5}} \quad [\mathrm{kN/m^2}], \quad t \leq \bar{t},$$
$$\eta = \omega_r t - 3\sqrt{6}, \quad \bar{t} = \frac{6\sqrt{6}}{\omega_r}, \tag{44}$$

where $\omega_r = 2\pi f$ denotes the central frequency of the pulse signal.

The theoretical wave speed[5] of the wave motion $u(x,t)$ in the third layer of this coupled-poroelastic-elastic-layers system is $v_{p(\text{poroelastic})}^{(\text{theoretical})} = 1683.7$m/s. The theoretical wave speed value is fairly close to the one computed from the numerical solution: the finite element solution, as illustrated in Figure 6, yields $v_{p(\text{poroelastic})}^{(\text{numerical})} = 1666.6$ m/s, which is only 0.97% smaller than the theoretical value (1683.7m/s). As seen in Figure 6, the wave speed $v_{p(\text{poroelastic})}^{(\text{numerical})} = 1666.6$ m/s, corresponding to $u(x,t)$, within the poroelastic third layer of the coupled-poroelastic-elastic-layers system is greater than its counterpart (1500 m/s) of the elastic third layer (with the same values of E, ν, and ρ_s) of the all-elastic-solid-layers system.[6]

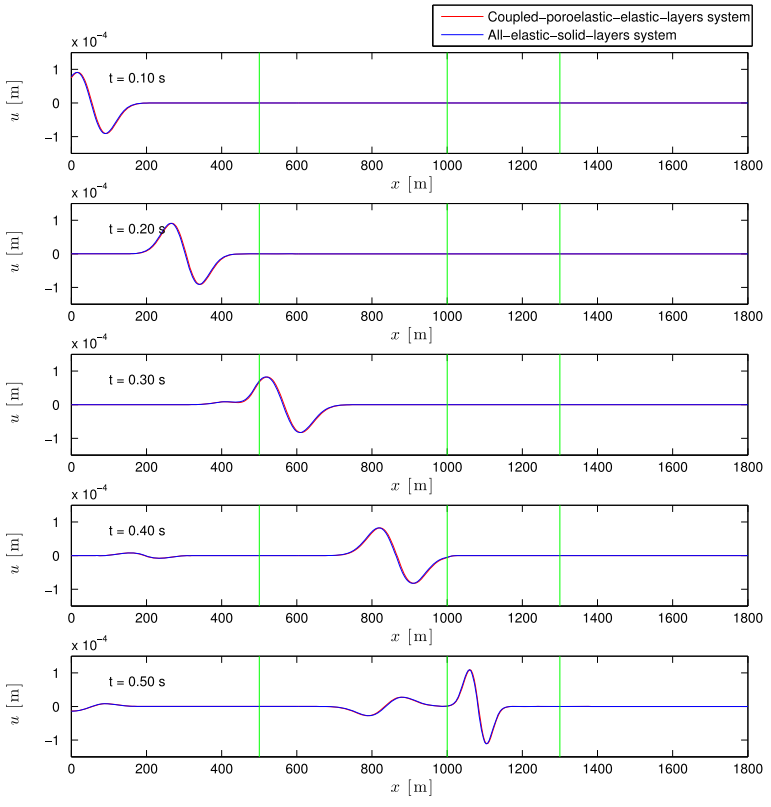

Figure 9. Comparison of the numerical solution of $u(x,t)$ of the coupled-poroelastic-elastic-layers system employing $((n=\alpha)\rightarrow 0)$ with that of the all-elastic-solid-layers system, 0.1 s $\leq t \leq$ 0.5 s.

Table 1. Rock properties of the 4-layered coupled-poroelastic-elasticlayers system.

	Layer 1	Layer 2	Layer 3 (poroelastic)	Layer 4
Length [m]	500	500	300	500
E [N/m^2]	1.25×10^{10}	1.8×10^{10}	4.5×10^{9}	3.2×10^{10}
ν	0.0	0.0	0.0	0.0
ρ_s [kg/m^3]	2000	2000	2000	2000
ρ_f [kg/m^3]			860	
n			0.3	
α			0.667	
Q [N/m^2]			2.2×10^{9}	
7.0×10^8 K_D [N/m^2]			1.5×10^{9}	
K_s [N/m^2]			1.5×10^{9}	
K_f [N/m^2]			7.0×10^{8}	
η [cp]			5	
$\bar{k}$ [md]			100	

Figure 7 shows the relative displacement field of the pore-fluid wave motion $w(x,t)$. We note that the amplitude of $w(x,t)$ is nearly six orders of magnitude smaller than that of $u(x,t)$. Given such a low fluid mobility ($\bar{k} = 100$ md and $\eta = 5$ cp), the absolute fluid displacement, i.e. $u(x,t) + w(x,t)$, is almost identical to the rock matrix displacement

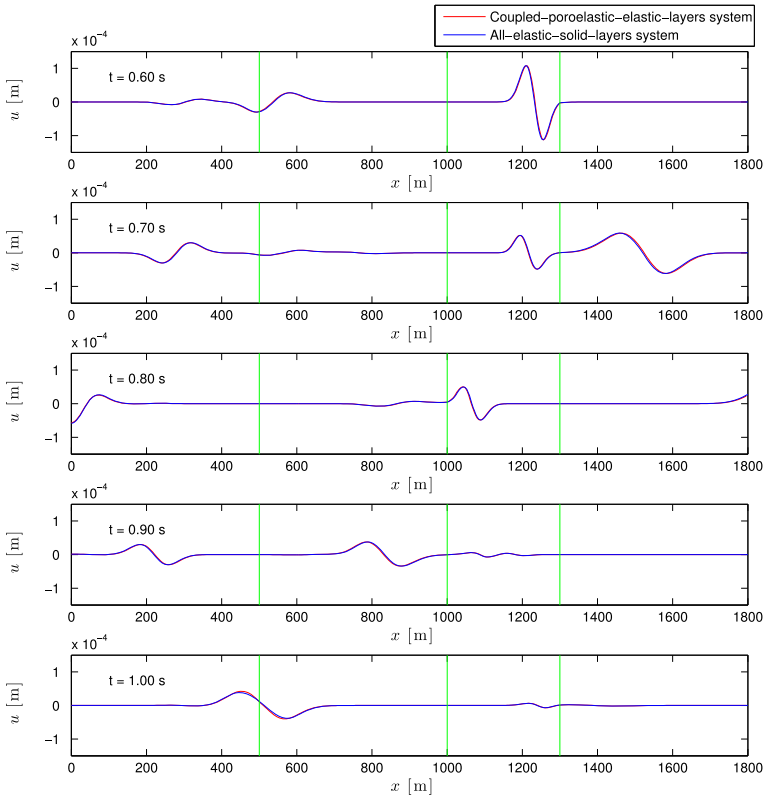

Figure 10. Comparison of the numerical solution of $u(x,t)$ of the coupled-poroelastic-elastic-layers system employing $((n = \alpha) \to 0)$ with that of the all-elastic-solid-layers system, 0.6 s $\leq t \leq$ 1.0 s.

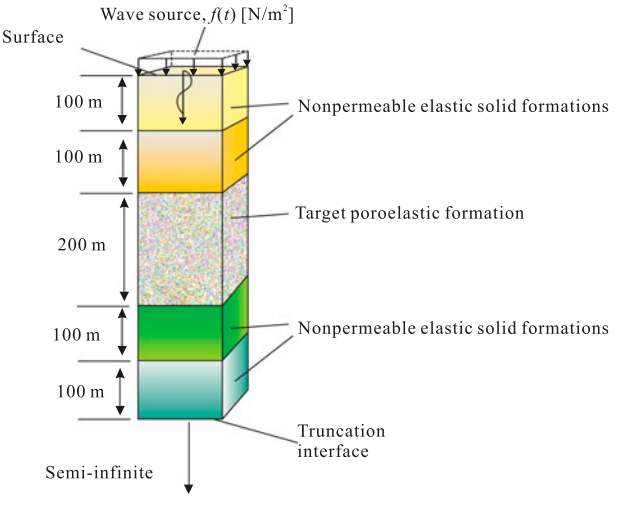

Figure 11. A five-layered system of a semi-infinite extent truncated at depth $x = 600$ m, with a poroelastic layer surrounded by non-permeable elastic solid layers.

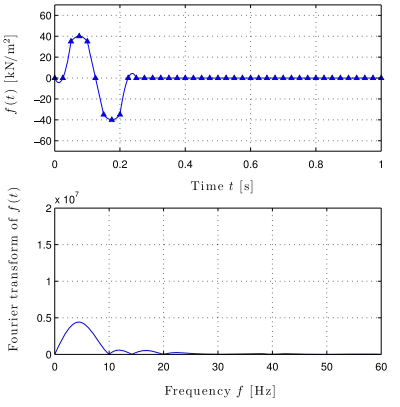

(a) The initially guessed loading signal $f(t)$

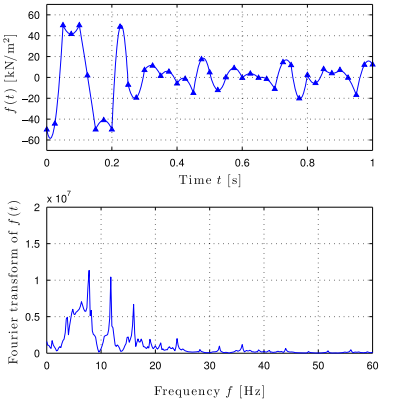

(b) The loading signal $f(t)$ after 8 iterations

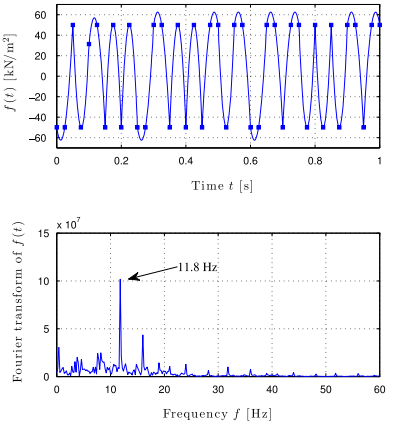

(c) The loading signal $f(t)$ finally converged after 40 iterations

Figure 12. An optimized loading signal at different iteration steps; the loading signal is discretized by using 100 quadratic shape elements for the observation time 5 s; the time signal is shown only up to 1 s.

$u(x,t)$ [92]. Meanwhile, Figure 8 shows that the order of magnitude of the amplitude of the pore pressure $P(x,t)$ (computed by using (5b)) is as large as that of the total stress field $\sigma(x,t)$ within the poroelastic layer in this example. It should be also noted that the continuity conditions of the solid displacement $u(x,t)$ and the total stress $\sigma(x,t)$ are satisfied at the interfaces between the poroelastic layers (Ω_p) and the elastic layers ($\Omega \setminus \Omega_p$), and the relative displacement of fluid $w(x,t)$ vanish at the interfaces. This observation suggests that the interface conditions between Ω_p and $\Omega \setminus \Omega_p$ are implemented correctly in the presented forward wave solver. For the verification of the presented FEM solution of the wave responses within the poroelastic layer, we compared the presented solution with its analytical counterpart [74], showing excellent agreement.

To further verify the modeling of the coupled-poroelastic-elastic-layers system, we note that the wave equations of the poroelastic layers (2) and (3) reduce to the equation of motion for an elastic solid, (1), provided that the porosity n and Biot's material parameter α, in (2) and (3), are equal to each other and approach zero, i.e. $(n = \alpha) \to 0$. Thus, the solution of the coupled-poroelastic-elastic-layers system, obtained by using (34) and

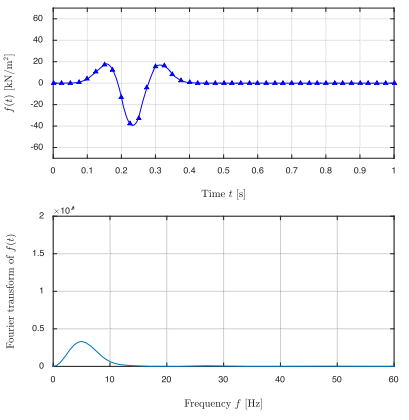

(a) The initially guessed loading signal $f(t)$

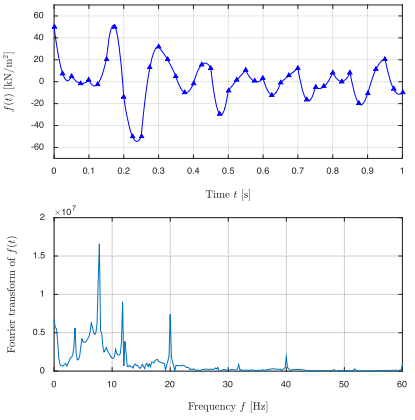

(b) The loading signal $f(t)$ after 8 iterations

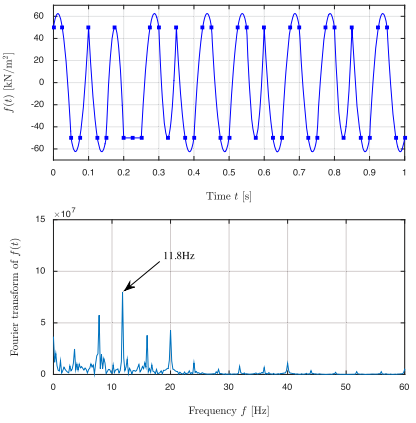

(c) The loading signal $f(t)$ finally converged after 40 iterations

Figure 13. An optimized loading signal at different iteration steps; a Ricker pulse signal with a 5 Hz central frequency is used as an initial guess; the loading signal is discretized by using 100 quadratic shape elements.

material parameters including $(n = \alpha) \to 0$, should match with that of a multi-layered system where all layers are occupied by elastic solids, provided that the two systems use the same values of E, ν, and ρ_s of all layers. To test this hypothesis, we obtain the numerical solution of the truncated four-layered coupled-poroelastic-elastic-layers system, whose third layer is a poroelastic layer (Figure 4). We use the material properties in Table 1 except for very small values of n and α, i.e. $n = \alpha = 1 \times 10^{-10}$, for the poroelastic layer. As seen in Figures 9 and 10, the comparison of the numerical solution of the coupled-poroelastic-elastic-layers system with that of the all-elastic-solid-layers system shows excellent agreement.

5.2. *Wave source optimal signals*

This subsection presents numerical experiments of the identification of the optimal loading time signals of a wave source, maximizing the kinetic energy in terms of $w(x, t)$ of the pore

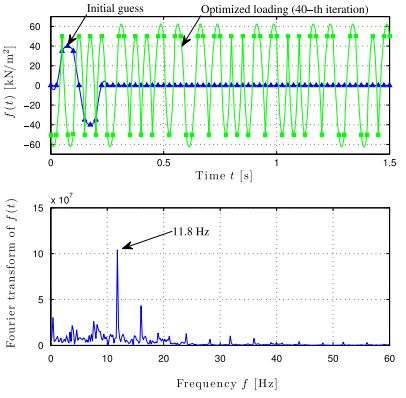

(a) The optimized $f(t)$ discretized by using 100 elements

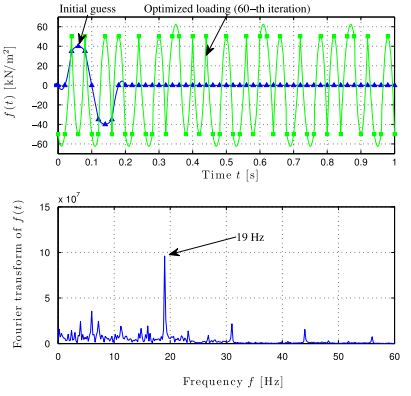

(b) The optimized $f(t)$ discretized by using 125 elements

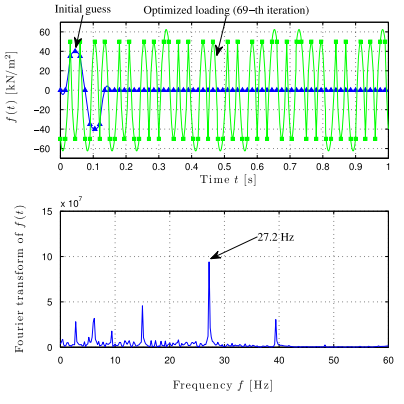

(c) The optimized $f(t)$ discretized by using 200 elements

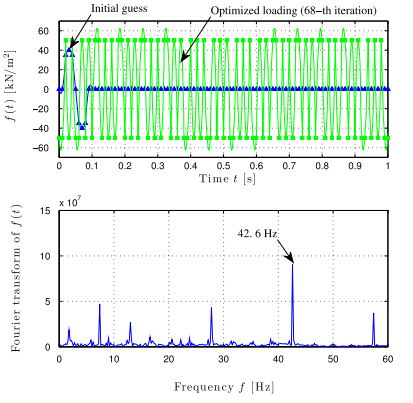

(d) The optimized $f(t)$ discretized by using 250 elements

Figure 14. Optimal loading signals that are finally converged via the minimization of (11) and the frequency spectra of the optimized loadings.

Table 2. Rock properties of the 5-layered subsurface formation system shown in Figure 11.

	Layer 1	Layer 2	Layer 3 (poroelastic)	Layer 4	Layer 5
Length [m]	100	100	200	100	100
E [N/m^2]	4.0×10^9	4.8×10^9	1.0×10^9	5.5×10^9	6.0×10^9
ν	0.2	0.2	0.2	0.2	0.2
ρ_s [kg/m^3]	2000	2000	2000	2000	2000
ρ_f [kg/m^3]			860		
n			0.3		
α			0.33		
Q [N/m^2]			2.2×10^9		
K_D [N/m^2]			5.6×10^8		
K_s [N/m^2]			8.3×10^8		
K_f [N/m^2]			7.0×10^8		
η [cp]			5		
$\bar{k}$ [md]			100		

fluid within a target poroelastic formation. The third layer is the targeted oil-saturated poroelastic formation, while the surrounding layers represent non-permeable elastic solid

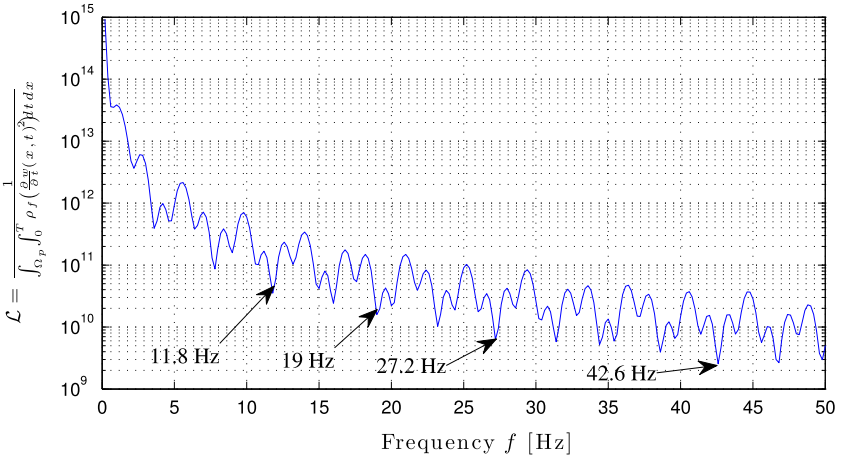

Figure 15. The distribution of the objective functional (11) with respect to frequencies $f = 0.1$–50 Hz for a sinusoidal excitation $f(t) = 50 \sin(2\pi ft)\text{kN/m}^2$ atop the 5-layered subsurface formation model in Figure 11; the optimization experiments recover a set of the amplification frequencies – 11.8, 19.0, 27.2, and 42.6 Hz – corresponding to strong local minima.

formations. We use the five-layer subsurface formation model shown in Figure 11. The material parameters of the formations are described in Table 2. We use a linear-linear element pair of element size 1m for the spatial approximation of both solutions $u(x,t)$ and $w(x,t)$. The objective functional (11) is minimized by using an initially-guessed perturbation-like non-periodic time signal with duration equal to 5 s. We require that the amplitude of each discretized force parameter (per (12)) does not exceed 50kN/m^2. Even though the excitation parameters do not exceed 50kN/m^2, the interpolated loading time signal can reach up to 60kN/m^2 (see Figures 12 to 14).[7] The total observation duration is $T = 5$ s, and the time step for resolving the state and adjoint problems is $\Delta t = 0.001$ s.

Figure 12(a) shows that the optimization process starts with an initially guessed sinusoidal-like loading signal, temporally discretized by using 100 quadratic elements.

The triangular symbols shown in Figure 12(a) represent the discretized force parameters utilized for the temporal approximation of a guessed loading time signal (we use these symbols in all similar plots in Figures 12 to 14). Figure 12(b) shows that the frequency spectrum of the guessed loading signal changes as the presented numerical optimizer updates the values of the discretized force parameters. After 40 iterations, the optimizer converges to the loading signal shown in Figure 12(c) with a strong dominant frequency of 11.8 Hz. It should be noted that the finally converged time signal shown in Figure 12(c) has a frequency spectrum, which differs significantly from that of the initially guessed signal: the optimization process begins by using a blind initial guess.

To explore the sensitivity of the converged signal to the initial guess, we repeated the previous numerical experiment, starting with a Ricker pulse, with a central frequency of 5 Hz, instead of the sinusoidal-like pulse. Figure 13 summarizes the results. Notice that the converged signal has frequency content similar to the one recovered with the sinusoidal-like pulse: in particular, as it can be seen in Figure 12(c), the dominant frequency of the converged signal's spectrum is again 11.8 Hz, the same dominant frequency as in the previous experiment. We conjecture that, as long as the spectrum of the initial guess is broad enough to contain the formation's amplification frequencies, the optimizer will

converge to a signal that will be revealing the amplification frequencies (provided that the mesh density can numerically support the frequencies).

Figure 14 demonstrates that the optimization procedures using initially guessed signals, discretized by using 100, 125, 200, and 250 elements, converge to time signals with dominant frequencies, 11.8, 19.0, 27.2, and 42.6 Hz, respectively. Each recovered frequency corresponds to one of the strong local minima of the frequency-sweep distribution of the value of the objective functional (Figure 15). Here, the frequency sweep is obtained by using a time-harmonic excitation $f(t) = 50 \sin(2\pi ft)\text{kN/m}^2$ with a frequency f varying from 0.1 to 50 Hz. Although the value of the objective functional, in the frequency sweep, tends to decrease as the frequency increases, there are a set of amplification frequencies corresponding to the strong local minima in the frequency sweep (Figure 15). These optimization experiments show that the dominant frequencies of the recovered optimal loading signals successfully recover the amplification frequencies, which can be otherwise obtained by the frequency sweep. Thus, we suggest that this optimization scheme is capable of recovering the essential characteristics of optimal wave sources for the wave-based EOR.

We remark that the minimization of the functional $\mathcal{L}$ of equation (11) is likely to produce a sinusoidal-like signal with a strong dominant frequency component, as was, in fact, shown in the numerical results. This is attributed to the one-dimensional character of the problem we considered. Despite the presence of layering, and the multiple reflections at the interface boundaries, in a one-dimensional setting there is only one propagation direction. By contrast, in higher spatial dimensions, the propagation path would depend on the heterogeneity of the formation, and transient signals that allow for the building of constructive interference at the target formation cannot be excluded. Though monochromatic solutions can still arise as the global optimum for the wave source signal in two or three dimensions, non-harmonic solutions are also possible. In short, in the problem under consideration, the optimizer will always converge to a signal whose spectrum will reveal strong discrete frequency components, whether the signal is monochromatic or not.

6. Conclusions

We described the mathematical and numerical modeling for identifying an unknown surface wave source's optimal loading signal that can maximize the relative wave motion of a single-phase pore fluid within a target poroelastic formation surrounded by non-permeable elastic solid formations of semi-infinite extent. At the heart of the modeling is a PDE-constrained-optimization-based numerical optimization scheme. The numerical experiments show that the suggested method can successfully recover optimal loading signals, whose spectrum contains dominant frequencies that coincide with the formation's amplification frequencies, and induce larger wave pore fluid relative motion than other signals. Thus, the optimization scheme is capable of recovering the essential temporal characteristics for a wave-based EOR.

This work could be extended into the more complicated yet realistic three-dimensional setting, where a fleet of downhole vibrators within horizontal wells, and/or ground surface sources are deployed. Then, the optimal conditions (e.g. the spatial distribution, the directions of excitational forces, and the loading time signals) of wave sources could maximize the amount of the vibrationally-mobilized oil, which can be estimated using a hysteretic model [93]. Our theoretical formulation could also be used to study the effect of a

fracture network (either naturally-existing or hydraulically-fractured) on the performance of the wave-based EOR.

Nomenclature

Symbol	Definition
x	Location
t	Time
x_i	Depth of a boundary or an interface atop the i-th layer
$x_p, x_{p+N_{\mathrm{pls}}}$	The locations of the two interfaces between the non-permeable elastic solid layers and the poroelastic layers
p	The layer index of the top poroelastic formation
L	The depth of absorbing boundary
Ω	Total coupled system $= (0, L)$
Ω_{p}	Poroelastic formations
$u_{\mathrm{a}}(x,t)$	Displacement of the non-permeable elastic solid formations
$u_{\mathrm{b}}(x,t)$	Displacement of solid rock matrix of the poroelastic formations
$w(x,t)$	Relative displacement of pore-fluid motion
$\sigma(x,t)$	Total stress
$\sigma'(x,t)$	Effective stress
$P(x,t)$	Pore pressure
N_{pls}	Total number of the poroelastic layers
N_{ls}	Total number of all layers
T	Total observation duration
E	Elastic modulus of elastic solid or rock matrix of poroelastic solids
λ	Lamé's first parameter of elastic solid or rock matrix of poroelastic solids
μ	Shear modulus of elastic solid or rock matrix of poroelastic solids
ν	Poisson's ratio of elastic solid or rock matrix of poroelastic solids
ρ	Mass density of elastic solid or fluid-solid mixture
ρ_s	Mass density of solid rock matrix
ρ_f	Mass density of pore fluid
k	Fluid mobility, i.e. $k = \bar{k}/\eta$, as shown by [83]
$\bar{k}$	Permeability
η	Viscosity of pore fluid
n	Porosity
α	Biot's parameter, i.e. $\alpha = 1 - \frac{K_D}{K_S}$, where $n \leq \alpha \leq 1$
Q	Biot's parameter, i.e. $Q = 1/\left(\frac{n}{K_f} + \frac{\alpha - n}{K_S}\right)$, where $0 < Q \leq \infty$
K_D	Bulk modulus of drained solid rock matrix, i.e. $K_D = \frac{E}{3(1-2\nu)}$
K_S	Bulk modulus of undrained solid rock matrix, i.e. $K_s = K_D/(1-\alpha)$
K_f	Bulk modulus of pore fluid
v_p	Compressional wave velocity
$s(x), v(x)$	Test functions
$f(t)$	Applied force of a surface wave source
n_f	Number of parameters for temporal discretization of $f(t)$
f_i	The i-th discretized force parameter for temporal approximation of $f(t)$
$\varphi_i(t)$	The i-th shape function for temporal approximation of $f(t)$
$\mathcal{L}$	Objective functional to be minimized
$\lambda_{u_{\mathrm{a}}}, \lambda_{u_{\mathrm{b}}}, \lambda_w$	Lagrange multipliers
λ_0, λ_L	Lagrange multipliers
$\mathcal{A}$	Lagrangian functional
δ	Variational symbol
$\mathcal{E}(\boldsymbol{x})$	Coefficient of the body force term of the adjoint PDE (refer to (16) and (17))
ξ	Control variable: $\xi = f_i$
$\mathbf{f}_{(k)}$	An array of force parameters at the k-th optimization iteration; see Algorithm 1
$\theta_{(k)}$	Step length at the k-th optimization iteration
α, β	Parameters of the optimization algorithm
f	Frequency of the loading time signal of a surface wave source

Notes

1. It should be noted that there have been source-inversion studies of different kinds reporting on identification of unknown spatial and/or temporal profiles of sources to systems by using sparsely-measured response of the system induced by the sources [57–60].
2. The coupled wave equations for poroelastic solids fully saturated by a single-phase fluid in the three-dimensional and one-dimensional settings are shown in [74,75] and,[73] respectively. The dimensional reduction from the three-dimensional equations to the one-dimensional equations is straightforward and omitted in this paper.
3. The total kinetic energy of the pore fluid at x and t is $\frac{\rho_f}{2}\left(\frac{\partial u}{\partial t}(x,t)+\frac{\partial w}{\partial t}(x,t)\right)^2$. Since we are interested in increasing the relative wave motion of the pore fluid, we maximize $\frac{\rho_f}{2}\left(\frac{\partial w}{\partial t}(x,t)\right)^2$, which is the kinetic energy only in terms of $w(x,t)$, the relative fluid displacement.
4. In this paper, λ with a subscript denotes a Lagrange multiplier, whereas λ without any subscript denotes the Lamé's first parameter.
5. We use $v_{p(\text{poroelastic})}^{(\text{theoretical})}=\sqrt{\frac{\lambda+2\mu+\alpha^2 Q}{\rho}}$. If there is a high viscosity-coupling between the solid rock matrix and the pore fluid within a poroelastic layer, then there is only one longitudinal wave of the speed, i.e. $v_{p(\text{poroelastic})}^{(\text{theoretical})}=\sqrt{\frac{\lambda+2\mu+\alpha^2 Q}{\rho}}$, within the poroelastic layer [91].
6. We obtain the FEM solution of the wave response of the all-elastic-solid-layers system, whose layering is identical to that of the coupled-poroelastic-elastic-layers system, except for the third layer that is replaced by an elastic solid layer. For this elastic wave solution, we use, again, the values of E, ν, and ρ_s for each layer shown in Table 1, the linear elements with element size 4m, and Δt of 0.001 s.
7. A modern Vibroseis can deliver dynamic pressure up to 60kN/m^2 (or more) to the ground surface [4].

Disclosure statement

No potential conflict of interest was reported by the authors.

Funding

This work was partially supported by an Academic Excellence Alliance grant between King Abdullah University of Science and Technology (KAUST) and the University of Texas at Austin and by the Society of Petroleum Engineers STAR Fellowship and the William S. Livingston Fellowship at the University of Texas at Austin awarded to the first author.

References

[1] Lakatos I. Global oil demand and role of chemical EOR methods in the 21st century. Int. J. Oil Gas Coal Technol. 2008;1:46–64.
[2] Lake LW. Enhanced oil recovery. Englewood Cliffs (NJ): Prentice Hall; 1989.
[3] Lake LW, Schmidt RL, Venuto PB. A niche for enhanced oil recovery in the 1990s. Schlumberger Oilfield Rev. 1992;4:55–61.
[4] Kalinski ME. Effect of vibroseis arrays on ground vibrations: a numerical study. J. Environ. Eng. Geophys. 2007;12:281–287.
[5] Fathi A, Kallivokas LF, Poursartip B. Full-waveform inversion in three-dimensional PML-truncated elastic media. Comput. Methods Appl. Mech. Eng. 2015;296:39–72.
[6] Kallivokas L, Fathi A, Kucukcoban S, et al. Site characterization using full waveform inversion. Soil Dyn. Earthquake Eng. 2013;47:62–82.
[7] Fathi A. Full-waveform inversion in three-dimensional pml-truncated elastic media: theory, computations, and field experiments [dissertation]. The University of Texas at Austin; 2015.

[8] Bremmer C, Harris G, Kosmala A, et al. Evolving technologies: electrical submersible pumps. Schlumberger Oilfield Rev. 2006:30–43.
[9] Paulsson BN. Nondestructive downhole seismic vibrator source and processes of utilizing the vibrator to obtain information about geologic formations. United States Patent 4805725. 1989.
[10] Westermark RK, Brett JF, Maloney DR. Enhanced oil recovery with downhole vibration stimulation. In: SPE Production and Operations Symposium, SPE 67303-MS. Oklahoma City (OK): Society of Petroleum Engineers; 2001.
[11] Osika DG. Fluid regime of seismically active regions (fluidniy rejim seismicheski-aktivnikh oblastey)(in Russian). Nauka Press; 1981.
[12] Smimova MN. Effect of earthquakes on the oil yield of the Gudermes field (Northeastern Caucasus). Izv. Aca. Sci., USSR, Fizika Zemli (Physics of the Solid Earth). 1968;12:71–76.
[13] Steinbrugge KV, Moran DF. An engineering study of the Southern California earthquake of July 21, 1952, and its aftershocks. Bull. Seismol. Soc. Am. 1954;44:279–283.
[14] Voytov GI, Osika DG, Grechukhina TG, et al. Some geological and geochemical consequences of the Daghestan earthquake of may 14. Trans. USSR Acad. Sci. Earth Sci. Sect. 1970;1972:576–579.
[15] Barabanov VI, Pavlov MV. Increasing oil production from depleted fields through seismic stimulation. First break. 2009;27:97–102.
[16] Guo X, Du Z, Li G, et al. High frequency vibration recovery enhancement technology in the heavy oil fields of China. In: SPE International Thermal Operations and Heavy Oil Symposium and Western Regional Meeting SPE 86956. Bakersfield (CA): Society of Petroleum Engineers; 2004.
[17] Kostrov S, Wooden W. In situ seismic stimulation shows promise for revitalizing mature fields. Oil Gas J. 2005:2–25.
[18] Kostrov S, Wooden W. Possible mechanisms and case studies for enhancement of oil recovery and production using in-situ seismic stimulation. In: SPE/DOE Symposium on Improved Oil Recovery SPE 114025. Tulsa (OK): Society of Petroleum Engineers; 2008.
[19] Kouznetsov OL, Simkin EM, Chilingar GV, et al. Improved oil recovery by application of vibro-energy to waterflooded sandstones. J. Pet. Sci. Eng. 1998;19:191–200.
[20] Kuznetsov OL, Simkin EM, Chilingar GV, et al. Seismic techniques of enhanced oil recovery: experimental and field results. Energy Source. 2002;24:877–889.
[21] Kuznetsov VV, Nikolaev AV. Elaboration of physical principles of vibro-seismic action on oil reservoir (razrabotka fizicheskikh osnov vibroseismicheskogo vozdeystviya na neftianouyou zalezh) Report (in Russian). Inst. Phys. Earth. 1990.
[22] Spanos T, Shand D, Davidson B, et al. Pressure pulsing at the reservoir scale: a new IOR approach. J. Can. Pet. Technology. 2003;42:16–28.
[23] Westermark RV, Brett JF, Maloney DR. Using downhole vibration stimulation for enhanced oil recovery. World Oil. 2001:57–66.
[24] Zhu T, Xutao H. Downhole harmonic vibration oil-displacement system: a new IOR tool. In: SPE Western Regional Meeting SPE 94001-MS. Irvine (CA): Society of Petroleum Engineers; 2005.
[25] Elkhoury JE, Brodsky EE, Agnew DC. Seismic waves increase permeability. Nature. 2006;441:1135–1138.
[26] Elkhoury JE, Niemeijer A, Brodsky EE, et al. Laboratory observations of permeability enhancement by fluid pressure oscillation of in situ fractured rock. J. Geophys. Res.: Solid Earth (1978–2012). 2011;116(B2).
[27] Geballe Z, Wang CY, Manga M. A permeability-change model for water-level changes triggered by teleseismic waves. Geofluids. 2011;11:302–308.
[28] Manga M, Beresnev I, Brodsky EE, et al. Changes in permeability caused by transient stresses: Field observations, experiments, and mechanisms. Rev. Geophys. 2012;50.
[29] Averbakh VS, Vlasov SN, Zaslavsky YM. Motion of a liquid droplet in a capillary under the action of static force and an acoustic field. Radiophys. Quantum Electron. 2000;43:142–147.
[30] Beckham RE, Abdel-Fattah A, Roberts PM, et al. Mobilization of colloidal particles by low-frequency dynamic stress stimulation. Langmuir. 2010;26:19–27.

[31] Beresnev IA, Johnson P. Elastic-wave stimulation of oil production: a review of methods and results. Geophysics. 1994;59:1000–1017.
[32] Hilpert M, Jirka GH, Plate EJ. Capillarity-induced resonance of oil blobs in capillary tubes and porous media. Geophysics. 2000;65:874–883.
[33] Amro MM, Al-Mobarky MA, Al-Homadhi ES. Improved oil recovery by application of ultrasound waves to waterflooding. In: SPE Middle East Oil and Gas Show and Conference, SPE 105370-MS. Kingdom of Bahrain: Society of Petroleum Engineers; 2007.
[34] Hamida T, Babadagli T. Capillary interaction of different oleic and aqueous phases between matrix and fracture under ultrasonic waves. In: SPE Europec/EAGE Annual Conference, SPE 94105. Madrid: Society of Petroleum Engineers; 2005.
[35] Hamida T, Babadagli T. Effect of ultrasonic waves on the capillary imbibition recovery of oil. In: SPE Asia Pacific Oil and Gas Conference and Exhibition, SPE 92124. Jakarta: Society of Petroleum Engineers; 2005.
[36] Hamida T, Babadagli T. Effects of ultrasonic waves on immiscible and miscible displacement in porous media. In: SPE Annual Technical Conference and Exhibition, SPE 95327. Dallas (TX): Society of Petroleum Engineers; 2005.
[37] Roberts PM, Abdel-Fattah AI. Seismic stress stimulation mobilizes colloids trapped in a porous rock. Earth Planet. Sci. Lett. 2009;284:538–543.
[38] Roberts PM, Esipov IB, Majer EL. Elastic wave stimulation of oil reservoirs: promising EOR technology? Leading Edge. 2003;22:448–453.
[39] Roberts PM, Sharma A, Uddameri V, et al. Enhanced DNAPL transport in a sand core during dynamic stress stimulation. Environ. Eng. Sci. 2001;18:67–79.
[40] Vogler ET, Chrysikopoulos CV. An experimental study of acoustically enhanced NAPL dissolution in porous media. Environ. Energy Eng. 2004;12:3271–3280.
[41] Thomas JM, Chrysikopoulos CV. Experimental investigation of acoustically enhanced colloid transport in water-saturated packed columns. J. Colloid Interface Sci. 2007;308:200–207.
[42] Iassonov PP, Beresnev IA. A model for enhanced fluid percolation in porous media by application of low-frequency elastic waves. J. Geophys. Res. 2003;108:2138–2146.
[43] Li W, Vigil RD, Beresnev IA, et al. Vibration-induced mobilization of trapped oil ganglia in porous media: Experimental validation of a capillary-physics mechanism. J. Colloid Interface Sci. 2005;289:193–199.
[44] Beresnev I, Gaul W, Vigil RD. Direct pore-level observation of permeability increase in two-phase flow by shaking. Geophys. Res. Lett. 2011;38.
[45] Beresnev IA. Theory of vibratory mobilization on nonwetting fluids entrapped in pore constrictions. Geophysics. 2006;71:47–56.
[46] Beresnev IA, Deng W. Viscosity effects in vibratory mobilization of residual oil. Geophysics. 2010;75:79–85.
[47] Deng W, Cardenas MB. Dynamics and dislodgment from pore constrictions of a trapped nonwetting droplet stimulated by seismic waves. Water Resour. Res. 2013;49:4206–4218.
[48] Jeong C, Huh C, Kallivokas LF. On the feasibility of inducing oil mobilization in existing reservoirs via wellbore harmonic fluid action. J. Pet. Sci. Eng. 2011;76:116–123.
[49] Jeong C, Kallivokas L, Kucukcoban S, et al. Maximization of wave motion within a hydrocarbon reservoir for wave-based enhanced oil recovery. J. Pet. Sci. Eng. 2015;129:205–220.
[50] Bachrach R, Nur A, Agnon A. Liquefaction and dynamic poroelasticity in soft sediments. J. Geophys. Res. 2001;106:13,515–13,526.
[51] Groenenboom J, Wong S, Meling T, et al. Pulsed water injection during waterflooding. In: International Improved Oil Recovery Conference in Asia Pacific SPE 84856. Kuala Lumpur: Society of Petroleum Engineers; 2003.
[52] Huh C. Improved oil recovery by seismic vibration: a preliminary assessment of possible mechanisms. In: International Petroleum Conference SPE 103870. Cancun: Society of Petroleum Engineers; 2006.
[53] Owens WW, Archer DL. Waterflood pressure pulsing for fractured reservoirs. J. Pet. Technol. 1966:745–752.

[54] Stirpe MT, Guzman MT, Manrique E, et al. Cyclic water injection simulations for evaluations of its potential in Lagocinco field. In: SPE/DOE Symposium on Improved Oil Recovery. Tulsa (OK): Society of Petroleum Engineers; 2004.
[55] Surguchev L, Koundin A, Melberg O, et al. Cyclic water injection: improved oil recovery at zero cost. Pet. Geosci. 2002;8:89–95.
[56] Allahverdiyev P. Improved sweep efficiency through seismic wave stimulation [master thesis]. The University of Texas at Austin; 2012.
[57] Sabelli A, Aquino W. A source sensitivity approach for source localization in steady-state linear systems. Inverse Prob. 2013;29:095005. Available from: http://stacks.iop.org/0266-5611/29/i=9/a=095005
[58] Akçelik V, Biros G, Ghattas O, et al. A variational finite element method for source inversion for convective-diffusive transport. Finite Elem. Anal. Des. 2003;39:683–705.
[59] Manesh MK, Hematiyan M, Eghtesad M, et al. Vibrating loads identification using inverse acoustics in fluid-structure interaction. Vol. 433, Advanced Materials Research. Trans Tech Publication; 2012. p. 51–57.
[60] Lloyd SF, Jeong C. Reconstruction of moving acoustic sources in a heterogeneous elastic solid. In: Society of Photographic Instrumentation Engineers (SPIE) 23rd Annual International Symposium on Smart Structures, Nondestructive Evaluation and Health Monitoring; 2016.
[61] Jeong C, Kallivokas LF, Huh C, et al. Optimization of sources for focusing wave energy in targeted formations. J. Geophys. Eng. 2010;7:242–256.
[62] Jeong C, Kallivokas LF, Huh C, et al. Maximization of oil mobility within a hydrocarbon reservoir for elastic wave-based enhanced oil recovery. In: SPE Annual Technical Conference and Exhibition; October 30-November 2; Denver (CO); 2011.
[63] Fathi A, Poursartip B, Kallivokas LF. Time-domain hybrid formulations for wave simulations in three-dimensional pml-truncated heterogeneous media. Int. J. Numer. Methods Eng. 2015;101:165–198.
[64] Kucukcoban S, Kallivokas LF. Mixed perfectly-matched-layers for direct transient analysis in 2D elastic heterogeneous media. Comput. Methods Appl. Mech. Eng. 2011;200:57–76.
[65] Kang JW, Kallivokas LF. Mixed unsplit-field perfectly matched layers for transient simulations of scalar waves in heterogeneous domains. Comput. Geosci. 2010;14:623–648.
[66] Lions J. Optimal control of systems governed by partial differential equations. Springer-Verlag; 1971.
[67] Karve PM, Kucukcoban S, Kallivokas LF. On an inverse source problem for enhanced oil recovery by wave motion maximization in reservoirs. Comput. Geosci. 2014;19:233–256.
[68] Karve PM, Kucukcoban S, Kallivokas LF. On an inverse source problem for enhanced oil recovery by wave motion maximization in reservoirs. Comput Geosci. 2015;19:233–256.
[69] Karve PM, Kallivokas LF. Wave energy focusing to subsurface poroelastic formations to promote oil mobilization. Geophys. J. Int. 2015;202:119–141.
[70] Karve PM, Kallivokas LF, Manuel L. A framework for assessing the uncertainty in wave energy delivery to targeted subsurface formations. J. Appl. Geophys. 2016;125:26–36.
[71] Biot MA. Theory of propagation of elastic waves in a fluid-saturated porous solid. I. Low-frequency range. J. Acoust. Soc. Am. 1956;28:168–178.
[72] Biot MA. Mechanics of deformation and acoustic propagation in porous media. J. Appl. Phys. 1962;33:1482–1498.
[73] Simon BR, Zienkiewicz OC, Paul DK. Evaluation of $u - w$ and $u - \pi$ finite element methods for the dynamic response of saturated porous media using one-dimensional models. Int. J. Numer. Anal. Methods Geomech. 1986;10:461–462.
[74] Simon BR, Zienkiewicz OC, Paul DK. An analytical solution for the transient response of saturated porous elastic solids. Int. J. Numer. Anal. Methods Geomech. 1984;8:381–398.
[75] Simon BR, Wu JSS, Zienkiewicz OC. Evaluation of higher order, mixed and Hermitean finite element procedures for dynamic analysis of saturated porous media using one-dimensional models. Int. J. Numer. Anal. Methods Geomech. 1986;10:483–499.
[76] Zienkiewicz OC, Shiomi T. Dynamic behavior of saturated porous media; the generalized Biot formulation and its numerical solution. Int. J. Numer. Anal. Methods Geomech. 1984;8:71–96.

[77] Al-Khoury R, Kasbergen C, Scarpas A, et al. Poroelastic spectral element for wave propagation and parameter identification in multi-layer systems. Int. J. Solids Struct. 2002;39:4073–4091.
[78] Kattis S, Beskos D, Cheng A. 2d dynamic response of unlined and lined tunnels in poroelastic soil to harmonic body waves. Earthquake Eng. Struct. Dyn. 2003;32:97–110.
[79] Degrande G, De Roeck G, Van den Broeck P, et al. Wave propagation in layered dry, saturated and unsaturated poroelastic media. Int. J. Solids Struct. 1998;35:4753–4778.
[80] Corapcioglu MY, Tuncay K. Propagation of waves in porous media. Adv. Porous Media. 1996;3:361–440.
[81] Berryman J, Thigpen L. Linear dynamic poroelasticity with microstructure for partially saturated porous solids. J. Appl. Mech. 1985;52:345–350.
[82] Auriault JL, Lebaigue O, Bonnet G. Dynamics of two immiscible fluids flowing through deformable porous media. Transp. Porous Media. 1989;4:105–128.
[83] Bourbie T, Coussy O, Zinszner B. Acoustics of porous media. Houston (TX): Gulf Publishing Company; 1987.
[84] Karush W. Minima of functions of several variables with inequalities as side constraints [master thesis]. Chicago (IL): The University of Chicago; 1939.
[85] Kuhn HW, Tucker AW. Nonlinear programming. In: Neyman J, editor. The Second Berkeley Symposium on Mathematical Statistics and Probability. University of California Press; 1951.
[86] Pakravan A, Kang JW. A gauss-newton full-waveform inversion for material profile reconstruction in 1d pml-truncated solid media. KSCE J. Civil Eng. 2014;18:1792–1804.
[87] Fletcher R, Reeves CM. Function minimization by conjugate gradients. Comput. J. 1951;7:149–154.
[88] Nocedal J, Wright S. Numerical optimization. New York (NY): Springer; 2006.
[89] Huang M, Zienkiewicz OC. New unconditionally stable staggered solution procedures for coupled soil-pore fluid dynamic problems. Int. J. Numer. Methods Eng. 1998;43:1029–1052.
[90] Newmark NM. A method of computation for structural dynamics. Proc. ASCE. 1959;85:67–94.
[91] Gajo A. Influence of viscous coupling in propagation of elastic waves in saturated soil. J. Geotech. Eng. 1995;121:636–644.
[92] Jeremić B, Cheng Z, Taiebat M, et al. Numerical simulation of fully saturated porous materials. Int. J. Numer. Anal. Methods Geomech. 2008;32:1635–1660.
[93] Jeong C, Huh C, Kallivokas LF, et al. Estimation of oil production rates in reservoirs exposed to focused vibrational energy. In: SPE Improved Oil Recovery Symposium. Tulsa (OK); 2014.